COMPRESSED SENSING DATA ACQUISITION AND RECONSTRUCTION FOR FAST PHOSPHORUS MAGNETIC RESONANCE SPECTROSCOPIC IMAGING

by

Gökçe Hale Hatay

Submitted to the Institute of Graduate Studies in

Science and Engineering in partial fulfillment of

the requirements for the degree of

Master of Science

in

Electrical and Electronics Engineering

Yeditepe University

2014

COMPRESSED SENSING DATA ACQUISITION AND RECONSTRUCTION FOR
FAST PHOSPHORUS MAGNETIC RESONANCE SPECTROSCOPIC IMAGING

APPROVED BY:

Asst. Prof. Dr. Esin Öztürk Işık   ....
(Supervisor)

Prof. Dr. Cem Ünsalan   ....

Prof. Dr. Haluk Küçük   ....

DATE OF APPROVAL: ../../2014

ACKNOWLEDGEMENTS

ABSTRACT

COMPRESSED SENSING DATA ACQUISITION AND RECONSTRUCTION FOR FAST PHOSPHORUS MAGNETIC RESONANCE SPECTROSCOPIC IMAGING

Brain is the most important organ for the human life, and therefore, brain tumors are among the tumors that are vital to diagnose, follow-up and treat. Magnetic Resonance Imaging (MRI) is the most commonly used imaging modality for diagnosis of brain tumors. Phosphorus MR spectroscopic imaging (^{31}P-MRSI) is a non-invasive metabolic imaging modality that can provide quantitative information about metabolism, energy and oxygen state, membrane synthesis and degradation, and pH of the tissue. ^{31}P-MR spectroscopic imaging cannot be practically used in clinical applications due to its extended acquisition times to enhance low phosphorus MR signal, despite all the important information it provides. To accelerate the acquisition process of MR, compressed sensing method has recently been used. Due to its denoising effect, compressed sensing does not reduce the signal to noise ratio (SNR).

This study aims to use compressed sensing to reduce the acquisition time of ^{31}P-MRSI in clinical applications. Initially, required parameters and undersampling patterns were analyzed and optimal values were determined for accelerating the ^{31}P-MRSI data acquisition with compressed sensing, using simulations. Using Philips Paradise environment, a ^{31}P-MR spectroscopic imaging pulse sequence was implemented for accelerating the data acquisition with compressed sensing, and this pulse sequence was integrated into a 3T Philips MR scanner. A volunteer and a brain tumor patient, who gave their informed consent, were scanned. The signal to noise ratio, peak heights and ratios were compared between accelerated and full k-space data using Bland Altman statistical test. Using Wilcoxon rank sum test, differences of spectral peak heights and ratio between the healthy and tumor tissue were observed for both full and compressed sensing datasets. This study showed that compressed sensing reconstruction could be used to accelerate ^{31}P-MR spectroscopic imaging of human brain and brain tumors.

ÖZET

HIZLI FOSFOR MANYETİK REZONANS SPEKTROSKOPİK GÖRÜNTÜLEME İÇİN SIKIŞTIRILMIŞ ALGILAMA İLE VERİ ALIMI VE GERİ ÇATMA

Beyin, insanın hayatını devam ettirebilmesi için gereken en önemli organdır. Beyin tümörleri bu yüzden teşhisi, tedavisi ve takibi önemli tümörler arasında yer almaktadır. Beyin tümörleri teşhisinde ve konumunun belirlenmesinde manyetik rezonans görüntüleme (MRG) en yaygın olarak kullanılan görüntüleme tekniğidir. Fosfor MR spektroskopik görüntüleme (^{31}P-MRSG) dokunun metabolizması, enerji ve oksijen durumu, membran sentezi ve yıkımı, ve pH değeri hakkında kantatif bilgi sağlayan bir non-invaziv metabolik görüntüleme tekniğidir. ^{31}P-MRS görüntüleme sağladığı önemli bilgilere rağmen düşük fosfor MR sinyalini iyileştirmek için uzatılan veri alım süresinden dolayı klinikte yaygın olarak kullanılamamaktadır. MR veri alımını hızlandırmak için gürültü azaltım işlevi görmesi ve bu sayede sinyal gürültü oranını (SGO) düşürmediğinden dolayı sıkıştırılmış algılama yöntemi kullanılmaya başlanmıştır.

Bu çalışmada sıkıştırılmış algılama kullanılarak klinikte ^{31}P-MR spektroskopik görüntülemenin hızlandırılması hedeflenmektedir. Öncelikle simülasyon çalışmaları ile sıkıştırılmış algılama yöntemiyle ^{31}P-MR spektroskopik veri alımının hızlandırılması için gerekli parametreler ve altörnekleme düzenleri analiz edildi ve en uygun değerler tespit edildi. Philips Paradise sistemi kullanılarak sıkıştırılmış algılama yöntemiyle hızlandırılmış ^{31}P-MR spektroskopik görüntüleme darbe sekansı programlandı ve 3T Philips MR tarayıcısına kuruldu. Çekim alınmasına izin veren sağlıklı bir gönüllü ve beyin tümörlü bir hastadan veriler alındı. Hızlandırılmış ile tam k-uzayı verileri, arasındaki SGO değerleri, pik yükseklikleri ve oranları farklılıkları Bland Altman testi kullanılarak istatistiksel olarak karşılaştırıldı. Wilcoxon sıra toplam testi kullanılarak ise hastalarda sağlıklı ve tümörlü doku arasındaki pik yükseklik ve oran farklılıkları tam ve sıkıştırılmış algılama verileri için incelendi. Bu çalışma, sıkıştırılmış algılama yönteminin insan beyninin ve tümörlerin fosfor manyetik rezonans spektroskopi ile görüntülenmesini hızlandırmak için kullanılabileceğini göstermiştir.

TABLE OF CONTENTS

LIST OF FIGURES

LIST OF TABLES

LIST OF ABBREVIATIONS

CT   Computed Tomography

MRI   Magnetic Resonance Imaging

MRSI   Magnetic Resonance Spectroscopic Imaging

^{1}H-MRSI   Proton Magnetic Resonance Spectroscopic Imaging

^{13}C-MRSI   Carbon Magnetic Resonance Spectroscopic Imaging

^{31}P-MRSI   Phosphorus Magnetic Resonance Spectroscopic Imaging

ISIS   Image Selected In vivo Spectroscopy

FID   Free Induction Decay

RF   Radio Frequency

PA   Pulse and Acquire

PC   Phosphorylcholine

PE   Phosphoethanolamine

GPE   Glycerophosphoethanolamine

GPC   Glycerophosphorylcholine

PCr   Phosphocreatine

Pi   Inorganic phosphate

PDE   Phosphodiesterase

PME   Phosphomonoesterase

SNR   Signal to Noise Ratio

CS   Compressed Sensing

TR   Repetition Time

TE   Echo Time

2D CS   2D Iterative Frame Based Compressed Sensing Reconstruction

3D CS   3D Direct Compressed Sensing Reconstruction

1. INTRODUCTION

Brain tumors are among tumors that affect the human life negatively, and are important to diagnose and follow-up. The most commonly used clinical imaging technique to scan brain tumors is magnetic resonance imaging (MRI). MR spectroscopic imaging can provide further information about location and characteristics of brain tumors [1]. Due to the presence of high proton (^{1}H) content in human body, proton MR spectroscopic imaging (^{1}H-MRSI) is a commonly used MR spectroscopic imaging technique. Another non-invasive MR spectroscopic imaging technique is phosphorus MR spectroscopic imaging (^{31}P-MRSI), which detects the phosphorus containing metabolites in the brain. Quantitative information about energy metabolism, oxygen state, and pH of the tissue can be obtained using ^{31}P-MRSI [2]. Phosphocreatine (PCr), phosphorylcholine (PC), phosphoethanolamine (PE), inorganic phosphate (Pi), glycerophosphoethanolamine (GPE), glycerophosphorylcholine (GPC), β-ATP, α-ATP, and γ-ATP peaks are the main metabolite peaks that are detected by ^{31}P-MRSI.

The previous studies have shown that normal brain tissue and brain tumors have different phosphorus metabolite levels [2, 3]. Increase in phosphomonoesterase (PME) that is measured as the combined signal of PE and PC, and phosphodiesterase (PDE) that is measured as the combined signal of GPE and GPC are indicators of increase in membrane synthesis, and degradation, respectively. A decrease in PCr, and an increase in Pi/PCr, and β-ATP/PCr ratio in ^{31}P-MRSI [3] and a lactate peak in ^{1}H-MRSI [4] were observed when the brain tissue got ischemic. Hubesch et al. observed an increase in pH levels [2]. Maintz et al. observed an alkaline environment and a decrease in PCr and PDE peaks in meningiomas, and a slight alkalization and a reduction in PDE/α-ATP by more than twofold in low and high grade gliomas [3].

Phosphorus MR spectroscopy provides important information about brain tumor biochemistry; however this technique is not practical enough to be commonly used in clinical settings, due to the low phosphorus MR signal, and long acquisition times. A number of methods were developed to accelerate ^{31}P-MRS data acquisition. Echo planar spectroscopic imaging (EPSI) for fast ^{31}P-MRS data acquisition, needs high-powered

gradients, and the necessary pulse sequence is not readily available in clinical settings. Additionally, SNR losses might occur as a result of regriding errors [5, 6]. Another acceleration technique is generalized autocalibrating partially parallel acquisition (GRAPPA) that needs multi-channel phosphorus sensitive RF coils [7]. However, these coils are not available in vast majority of clinical MR scanners, and another problem is lower SNR, which is directly proportional to the square root of the data acquisition time.

Compressed sensing (CS) is a data acquisition and reconstruction method that has been used to accelerate MR data acquisition in recent years. Due to its denoising effect, compressed sensing can accelerate MR data acquisition with a lower SNR loss relative to the other fast imaging methods. Compressed sensing technique reconstructs randomly undersampled k-space data, and it was successfully applied for fast carbon MR spectroscopic imaging (^{13}C-MRSI) [8-10] and ^{31}P-MR spectroscopic imaging [11, 12]. In this study, we have assessed the feasibility of compressed sensing data acquisition and reconstruction for faster ^{31}P-MR spectroscopic imaging of human brain tumors.

2. BACKGROUND

2.1 BRAIN TUMOR

A brain tumor is localized intracranial lesion which occupies space within the skull and tends to cause a rise in intracranial pressure. Symptoms and signs seen in brain tumor patients can be common among those who suffer this condition, or can be very specific to the individual patients. These may include headaches, seizures, personality changes or memory loss, nausea or vomiting and fatigue.

There are two types of tumors, which are benign (noncancerous) and malignant (cancerous) tumors. Benign tumors can be removed and seldom grow back. The edge of the tumor can be seen clearly in the brain by using various medical imaging methods. Also, benign tumors cannot spread to other part of the body and they rarely invade other tissue around themselves. On the other hand, malignant brain tumors often threaten the person's life, grow rapidly and invade healthy brain tissue. Also, malignant brain tumors can spread to other parts of the brain or to the spinal cord.

In addition to the classification of brain tumors, tumor grade plays an important role for the survival of a person. There are four tumor grades, which are grade I, grade II, grade III and grade IV. Grade IV tumors tends to grow quickly and on claim the patient's life. Figure 2.1 shows magnetic resonance (MR) images of a healthy brain, and grade II and grade IV brain tumors.

Computed tomography (CT) and magnetic resonance imaging (MRI) are the most commonly used imaging techniques to diagnose brain tumors. CT can be helpful in diagnosing some types of brain tumors, especially those near or inside the bone. Also, CT can detect swelling, bleeding, and bone and tissue calcification. On the other hand, MRI technique is the best type of imaging with its superior soft tissue contrast, to diagnose brain tumors.
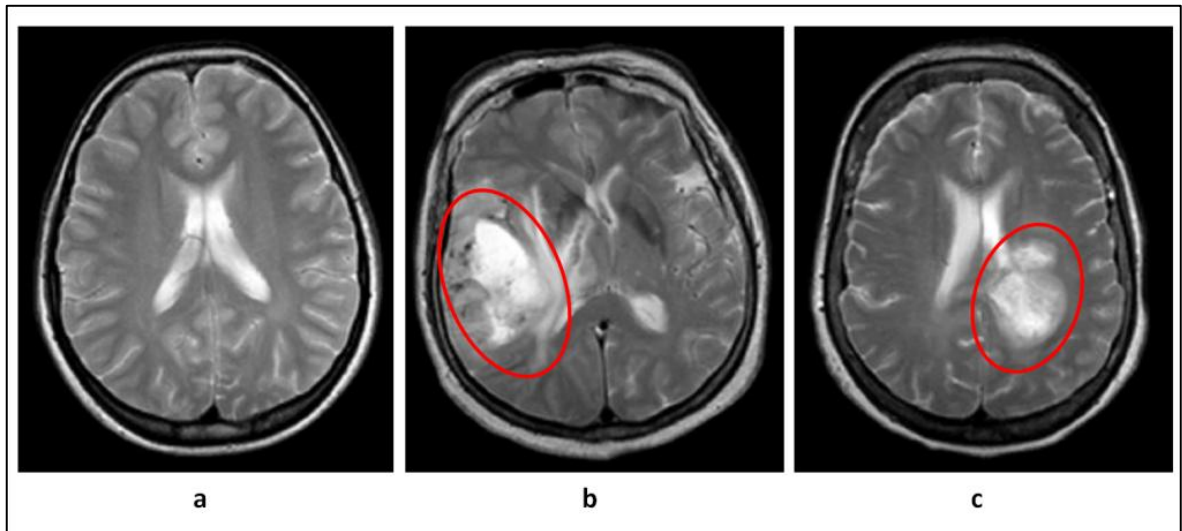
Figure 2.1 MR images of **(a)** a healthy brain, and **(b)** Grade II, **(c)** Grade IV brain tumors.

2.2   MAGNETIC RESONANCE IMAGING

Magnetic resonance imaging is a preferred medical imaging modality that is neither invasive nor dependent on harmful X-rays used in certain other imaging methods. Magnetic resonance imaging technology takes advantage of the possibility of causing a magnetic response from protons, by exposing them to magnetic fields with specific frequencies, which causes protons to resonate with that specific frequency. The resonance response caused by this application is then, measured by MRI hardware, and interpreted as in vivo images. [13]

Magnetic resonance imaging has exceptionally high soft tissue contrast, which makes this method vital for many in vivo imaging applications. However, it is not a perfect imaging method, primarily due to the comparatively longer acquisition times required to achieve a high spatial resolution and signal to noise ratio (SNR). There is a certain correlation between these three parameters and in order to shorten the data acquisition time, and make this modality more feasible for clinical use, spatial resolution and SNR must be sacrificed to a certain degree. [14]

An MRI system consists of four parts, which are magnet system, gradient system, radio frequency (RF) system, and computer. The purpose of the magnet system is to create a

uniform magnetic field, B_0. The direction of acquisition is determined by X, Y, Z gradients. Gradients are the coils that can help with determining the positions of protons of the tissue that is being imaged. A coil is an electromagnetic component that creates a specific magnetic field when powered by electricity. The coils are the primary components of an MRI scanner, since the technique itself relies on controlled magnetic fields. Most commonly used magnet type in a modern MRI scanner is a superconducting electromagnet, which is a niobium alloy material magnet, working at nearly 0 K and becomes a superconductor under these conditions. Superconductivity of the magnet allows it to reach extremely high magnetic field strengths. Figure 2.2 shows the gradient coils of an MR scanner.
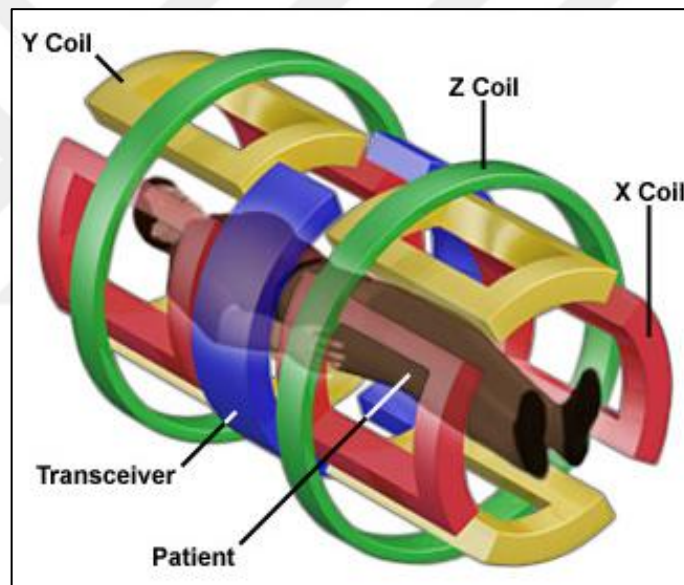
Figure 2.2 Gradient coils of an MR scanner. [15]

Spatial encoding involves three gradient coils, and each performs a specific encoding. First step is slice selection. The slice selection gradient is applied perpendicularly to the target plane. Since this RF pulse will only excite the protons on that specific slice, only a slice of the whole subject will give out a signal. Thickness of this slice is adjustable via the bandwidth of the RF pulse and the power of the gradient. Phase encoding gradient is applied vertically, and it alters the frequency of the protons it affects. This frequency alteration will persist after the RF pulse stops. The altered resonance frequency will result in a phase shift in the signal received from that specific group of protons, therefore creating another distinctive signal group, creating a second dimension in the image. Frequency

encoding gradient is the final step in spatial encoding. It assigns a certain resonance frequency to columns perpendicular to the ones created with phase encoding gradient. This causes every column to have separate distinguishable resonance frequency. By the end of this trio of encoding steps, every voxel will have a specific frequency and phase, that can be used to distinguish the source of incoming resonance signals by using a Fourier transform.

Magnetized protons have relaxation times, which are the time it takes for them to return to equilibrium. T1 is the longitudinal relaxation and T2 is the transverse relaxation time. Different tissues have different relaxation parameters and therefore by prioritizing a specific relaxation time, specific tissues can be inspected with MRI. The magnetic wave that initiates the particle resonance in the tissue is called the RF pulse. This magnetic pulse is of the same frequency with the Larmor frequency of the tissue. Because of the slightly different magnetic fields, protons in the tissue have slightly different spin characteristics. Main magnetic field is intentionally disturbed in a specific way by the gradient coils, and this results in free induction decay (FID). The time difference between the signal maximum and RF pulse application is called the Echo Time, and is denoted as TE. The repetition time of the whole process is denoted as TR. [16]

2.3 MAGNETIC RESONANCE SPECTROSCOPIC IMAGING

Magnetic resonance spectroscopic imaging (MRSI) is a non-invasive imaging technique that employs the same technology used in modern MRI systems. MRSI uses induced magnetic fields to trigger a magnetic resonance in the atomic particles that have the same Larmor frequency as the applied magnetic field. MRSI acquisitions are carried out with the MRI acquisition itself, and a spatial image that also has the frequency information of important metabolites is constructed using these acquisitions. In addition to the regular MRI data that is used to construct a spatial image of the area of interest, MRSI also acquires information of several metabolites that exist in the tissue, to determine the biochemical activity in specific areas, and allow the diagnosis of a possible tumor to be made with greater certainty.

Proton (^{1}H), phosphorus (^{31}P), carbon (^{13}C), sodium (^{23}Na), potassium (^{39}K) and fluorine (^{19}F) are the primary nuclei that MRS can detect in tissues [17]. The most commonly used MRSI technique is ^{1}H-MRSI, due to the vast availability of protons in human body. Choline (Cho), creatine (Cr), and N-acetyl aspartate (NAA) are the three major metabolite peaks that ^{1}H-MRSI can detect in the brain. Cho, Cr, and NAA provide information about membrane synthesis and degradation, energetic state, and neuronal activity, respectively. Increase in Cho peak and decrease in NAA peak are usually observed in tumor tissues [1]. Lipid and lactate peaks are observed at the same frequency in tumor tissue. Lipid can be seen in necrosis tissues, and lactate can be observed in case of lack of oxygenation. ^{1}H-MRSI provides vast amount of information, but is a difficult method due to the need of water suppression, and lipid signal problems caused by fatty tissue surrounding the brain [18]. For NAA amount to be correctly measured, lipid suppression [18, 19] or reduction of the lipid with processing methods after data acquisition [20] were previously employed.

Carbon MR spectroscopic imaging (^{13}C-MRSI) is another MR spectroscopic imaging method that allows the metabolic rate and mechanism to be understood in tumors [21, 22]. ^{13}C-pyruvate substrate labeled with hyperpolarized ^{13}C compound can be dynamically observed as it changes into lactate, alanine and bicarbonate, during the MR data acquisition [21-24]. ^{13}C-MRSI detects the carbon-labeled compound to understand metabolic rate of tumors and it is an expensive method.

The other commonly used MRSI method is phosphorus MR spectroscopic imaging (^{31}P-MRSI) which provides particular information about membrane degradation and synthesis, and energy metabolism of the tissue. ^{31}P-MRSI has certain advantages over ^{1}H-MR spectroscopic imaging, such as, ^{31}P-MRSI does not require any water suppression, and does not have any lipid contamination problems. ^{1}H-MR spectroscopy needs spectral editing techniques to measure lactate [25], however ^{31}P-MR spectroscopy can easily provide information about ischemic state of tissue with the measurement of PCr, Pi and β-ATP peaks. Tumor growth is related to both increased cell membrane synthesis and increased cell membrane degradation [26]. Although membrane synthesis and degradation is observed by a single Cho peak in ^{1}H-MR spectroscopy, these two mechanisms can be distinguished by using ^{31}P-MR spectroscopy. PME and PDE level changes point out

membrane synthesis and degradation. Three spectra samples of proton, carbon and phosphorus MR spectroscopic imaging are shown in Figure 2.3.
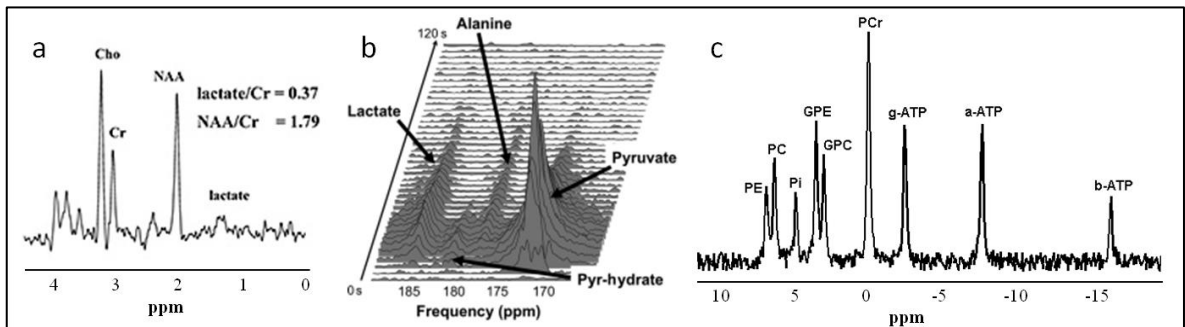
Figure 2.3 **(a)** ^{1}H-MRSI [27], **(b)** ^{13}C-MRSI [21], and **(c)** ^{31}P-MRSI spectra samples

2.4 PHOSPHORUS MAGNETIC RESONANCE SPECTROSCOPIC IMAGING

Phosphorus MR spectroscopic imaging (^{31}P-MRSI) is a type of non-invasive MR spectroscopic imaging method that detects the phosphorus containing metabolites instead of proton in the tissue. ^{31}P-MRSI can provide quantitative information about the energetic and ischemic state, membrane degradation and synthesis, and pH of the tissue of interest [2]. In phosphorus magnetic resonance spectroscopic imaging, phosphorylcholine (PC), phosphoethanolamine (PE), phosphocreatine (PCr), glycerophosphoethanolamine (GPE), glycerophosphorylcholine (GPC), inorganic phosphate (Pi), and β-ATP, α-ATP and γ-ATP peaks can be observed. PCr is seen as singlet at 0 ppm, and it is considered as a marker of phosphorylative energy metabolism and a reference peak of ^{31}P spectrum. Phosphorylcholine and phosphoethanolamine are phosphomonoesterase (PME) produced by phosphorylation of choline and ethanolamine, during membrane synthesis. Glycerophosphorylcholine and glycerophosphoethanolamine are formed during membrane degradation and the sum of these peaks is the phosphodiesterase peak (PDE). β-ATP peak is used to estimate ATP level, since there is no AMP and ADP contamination in it. In addition to metabolic information, intracellular pH level can be calculated by using frequency difference (d) between Pi and PCr peaks, with the following equation [3],

$$pH = 6.75 + \log\left[\frac{d - 3.27}{5.69 - d}\right]. \tag{2.1}$$

There is a difference between phosphorus metabolite levels of normal brain tissue and brain tumors, as shown by previous studies [2, 3]. When the ischemia forms in the brain tissue, ATP production occurs with hydrolysation of PCr by creatine kinase. ATP production results in a decrease in PCr, and increases in Pi/PCr and β-ATP/PCr, and an increase in pH level [2]. Increases in PME and PDE are signs of increase in membrane synthesis and degradation [3]. Maintz et al. evaluated the ^{31}P MR spectroscopic data of a large population of healthy volunteers, meningioma, and second, third and fourth grade brain tumor patients, and observed an alkaline environment (pH=7.16) as well as a decrease in PCr and PDE peaks in meningiomas, slight alkalization (pH=7.09) and a reduction in PDE/α-ATP by more than twofold in second, third and fourth grade gliomas [3]. Figure 2.7 shows 31P-MR spectra of tumor and healthy tissue that was acquired from a brain tumor patient diagnosed with non-Hodgkin's lymphoma (NHL). An increase in GPC and a decrease in PCr were observed in tumor region for this patient.
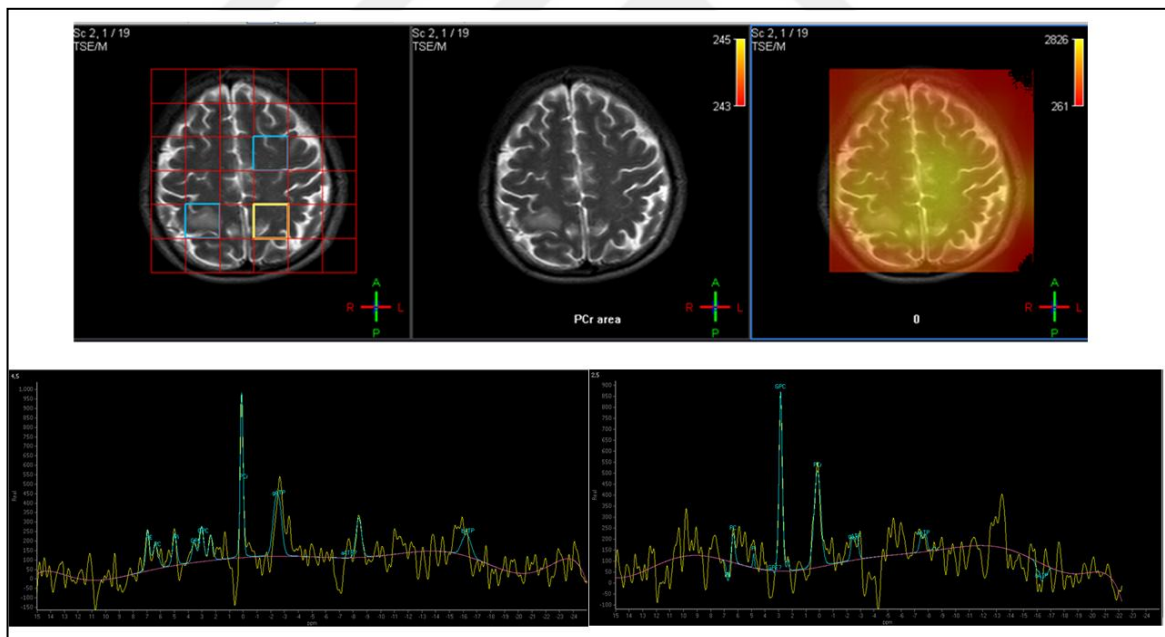
Figure 2.4 ^{31}P-MR spectra of a brain tumor patient who was diagnosed with NHL. The colored boxes represent selected spectra, left blue box and right spectrum being tumor and other two boxes and left spectrum being healthy.

2.4.1   IMAGE SELECTED IN VIVO SPECTROSCOPY

Image selected in vivo spectroscopy (ISIS) technique is widely used to acquire phosphorus MR spectroscopic signals that quickly decay due to low T2 relaxation values of phosphorus containing metabolites. In ISIS technique, free induction decay (FID) signal that occurs as a result of an RF pulse is acquired instead of echo signal which requires two or more RF pulses and longer TE time [28]. To be able to acquire MR signals originating from a specific region with ISIS, two or more signal are acquired, and by addition and subtraction of these signals from each, signals from the intended region can be estimated. Fundamentally, ISIS is a single voxel MR imaging method, and by using one dimensional ISIS a slice, two dimensional ISIS a column, and three dimensional ISIS a voxel can be selected.

To be able to select a single slice with one dimensional ISIS, which is the basic scenario, two separate measurements are needed as seen in Figure 2.4. In the first measurement, by using a 90° RF pulse without any location discrimination, all MR signals from the sensitivity region of the MR coil is tipped to the transverse plane and the signal is acquired. In the second measurement, before the 90° pulse, a 180° RF pulse along with a gradient in one direction is applied. The 90° pulse applied afterwards, tips the signal coming from the slice selected with the 180° pulse and the MR signal coming from out of this chosen slice, into transverse plane in opposing directions, and then the signal is acquired. By subtracting these two separate signal acquisitions and dividing the result by two, we get an approximate result of the MR signal coming from the targeted region.
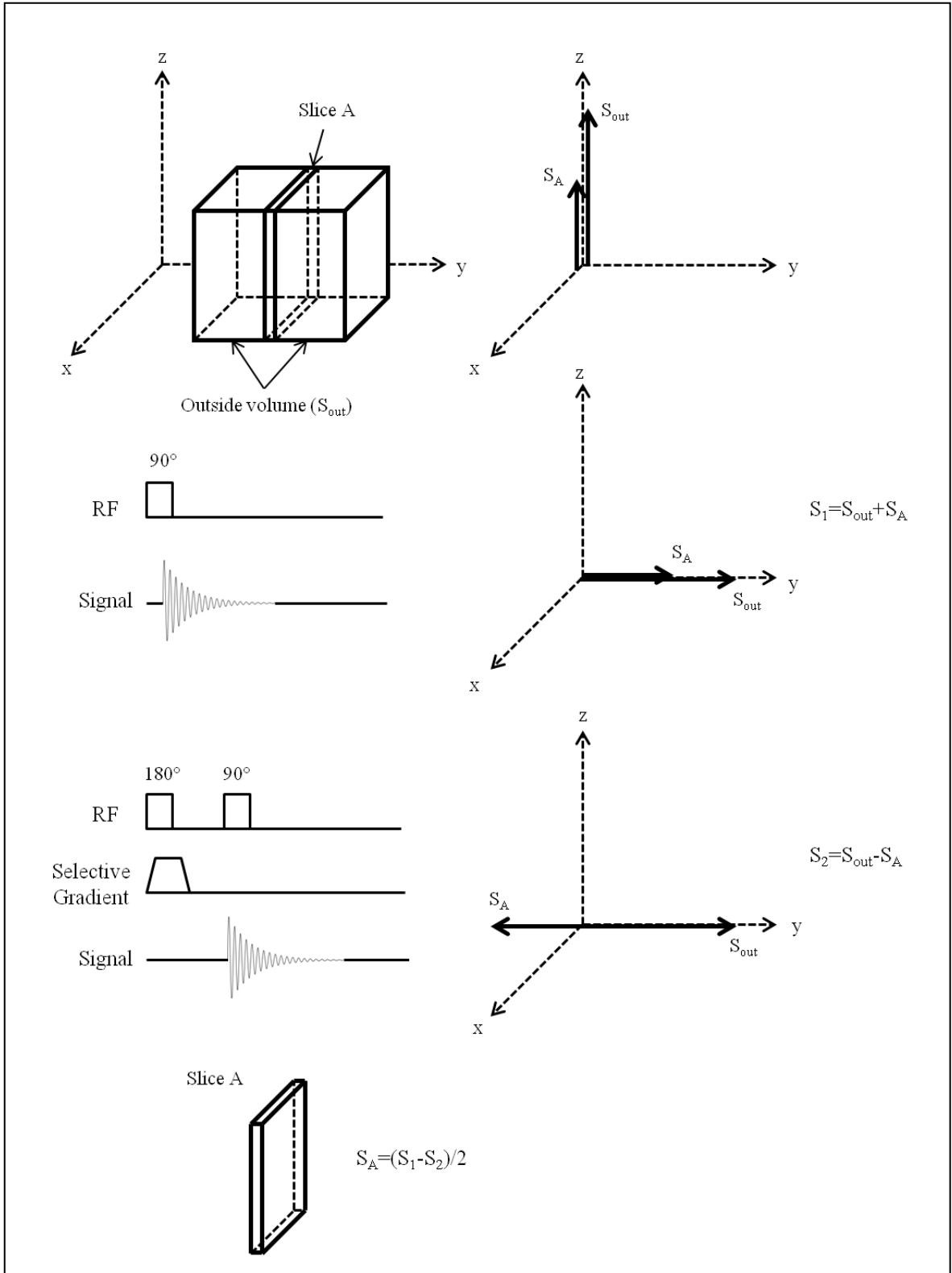
Figure 2.5 Selecting a slice with one-dimensional image selected in vivo spectroscopy technique.

For two dimensional signal localization with ISIS, gradients with two directions and four separate measurements, and for three dimensional localization, gradients with three directions and eight measurements are needed [29]. In Figure 2.5, gradient combinations of the 8 signals required for the selection of a voxel located at the intersection of A, B, C slices on the x, y, z planes, respectively, can be seen.
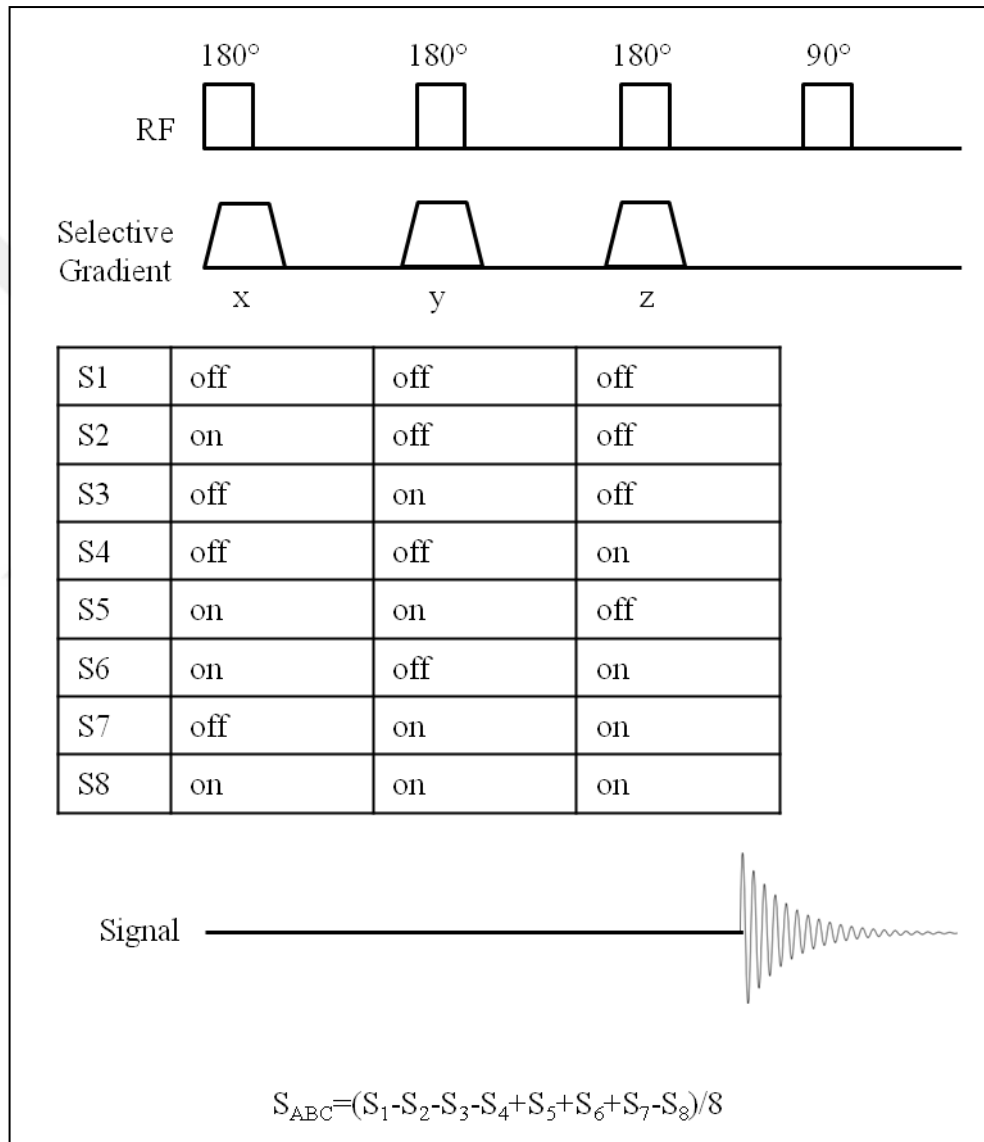
Figure 2.6 Necessary gradient combinations to acquire a single voxel that is located at the intersection of A, B, C slices on the x, y, z planes, respectively, with three-dimensional ISIS technique.

2.4.2   PULSE AND ACQUIRE

In pulse and acquire (PA) method, which acquires data in k-space and is used for MRS imaging, gradients are enabled in three directions, allowing for the selection of a voxel after an RF pulse. Data is acquired after the RF pulse and gradients are applied. A schematic of the first part of PA technique used in Philips MR scanner can be seen in Figure 2.6. In this figure, M, P, and S represent the 3 gradients in different directions. After the RF application, the gradients enable a phase difference in three planes, and data is collected from a point marked in k-space [29].
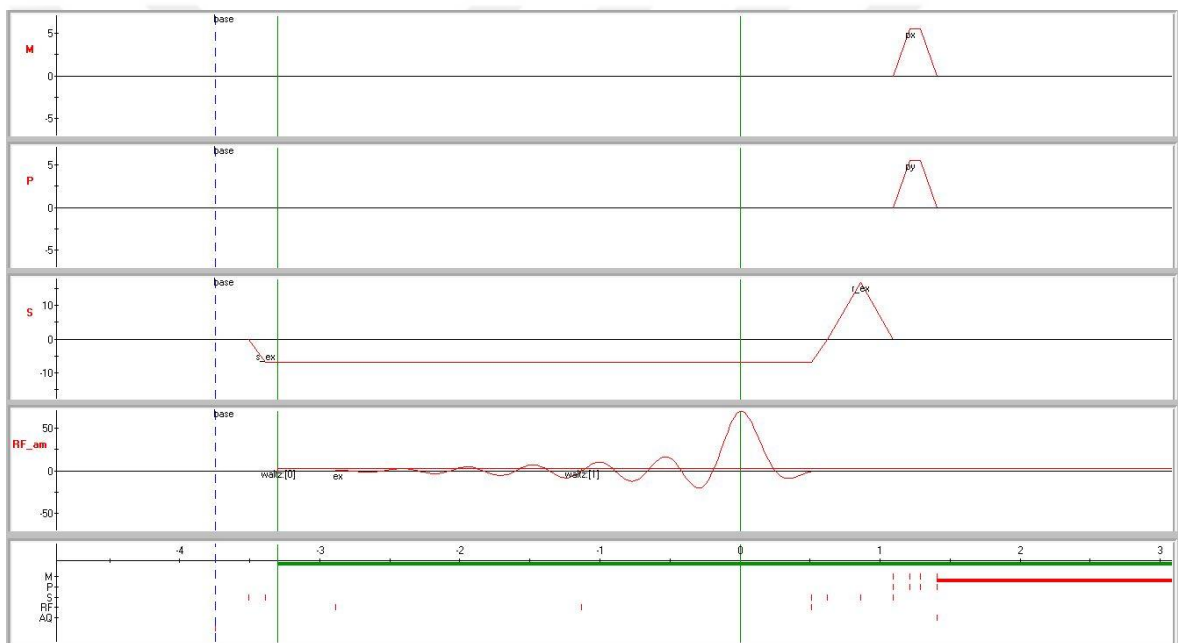
Figure 2.7 A schematic of the first part of a pulse and acquire sequence.

One of the problems with this method is the first order phase error caused by the time difference between RF application and data acquisition. When the pulse sequence was inspected, this timing difference was determined as 1.4072ms. The frequency of phosphorus is 51MHz at 3T (w=γB_0=17MHz/Tx3T=51MHz). The exponential equation below can be used to represent this first order error phase,

$$S = S_0 e^{-i2\pi(51*10^6 Hz)(1.4072x*10^{-3}s)}.$$ (2.2)

2.5   COMPRESSED SENSING TECHNIQUE

Compressed sensing technique was first discovered by Dr. Emmanuel Candes, with the help of Dr. Justin Romberg and Dr. Terence Tao, while he was working on noise reduction on a Shepp-Logan phantom by using L_1-norm reduction technique, and observed that the image was successfully and clearly reconstructed from a few samples [30-32]. This technique is based on the principal that randomly sampled sparse signals can be used to perfectly reconstruct the signal. Compressed sensing technique requires a) sparsity of signal in a transform domain, (in other words, signal should comprise a few non-zero components), b) random undersampling and incoherent aliasing in transform domain, and c) a non-linear reconstruction method, like conjugate gradient, to find an approximate solution for the ill-posed problem [33]. Lustig et al. used compressed sensing method to accelerate MR data acquisition, for the first time [33]. In this first application, MR contrast angiography images were accelerated with three dimensional MR imaging that are sparse in spatial domain, and fast spin echo MR images of the brain were also accelerated using compressed sensing method.

MR spectroscopic signals are sparse by their nature and throughout the spectral bandwidth, non-zero elements exist only at certain frequencies. Additionally a sparse MR spectroscopic signal can be correctly represented with a few large Wavelet components [9]. This fulfills the first criteria required to apply compressed sensing method. Secondarily, for the proper reconstruction of a signal of length N, and with M non-zero elements, at least K>MlogN individual samplings are needed [30]. The problem of reconstruction of randomly acquired time data in Fourier domain in all voxels by using compressed sensing can be formulated as [33],

$$
\begin{aligned}
&\min(\|\Psi(m)\|_1) \\
&\text{where } \|F_a(m) - y\|_2 < \varepsilon.
\end{aligned}
\tag{2.3}
$$

In this formula; m represents an approximate solution, $\psi(m)$ represents the Wavelet transform of this solution, F_a represents the undersampling operator in the Fourier space, y represents the original samples obtained from the signal, and ϵ represents the error margin

on the noise level. A low L_1-norm of the Wavelet transform means that the signal is sparse and can be calculated with the following formula,

$$\|x(i)\|_1 = \sum_i |x(i)|. \tag{2.4}$$

This difference and sparsity criteria can be transformed into Lagrange form and rewritten as an optimization problem as in equation 2.5. According to equation 2.5, the best solution must have its undersampled Fourier transform close to the original samples, and the signal formed must be sparse enough to be compressed with Wavelet transform.

$$\min_m \|F_a(m) - y\|_2 + \lambda \|\psi(m)\|_1. \tag{2.5}$$

Due to the limited number of samples in Fourier domain, MR reconstruction problem is an underdetermined one and multiple solutions exist. This causes the MR reconstruction problem to be ill posed [34]. For ill posed problems, an approximate solution is sought after by employing a priori information, or regularization techniques need to be used [35]. For the solutions of compressed sensing problems, conjugate gradient method which approximates a close solution is often employed.

2.5.1   Conjugate Gradient Method

Conjugate gradient method [36] is used to find an x value, that gives the minimum value for a second order function in the form of,

$$\eta_x = \frac{1}{2}x^T A x - b^T x + c. \tag{2.6}$$

In this equation, A is a real positive definite matrix. x value that gives the minimum value for this second order function also is the solution of Ax=b. Minimum point of the function η_x is where the gradient value is equal to zero, and the gradient of η_x is a vector that shows the direction where the growth of η_x is the greatest for any x [37]. The gradient of the function ηx is Ax-b.

The point where the gradient of η_x is equal to zero, is also the solution of Ax=b. A point, at where the minimum value of the second order function η_x is very close to the actual minimum, can be found using steepest descent method [37]. This method starts from a randomly selected x_0 point and iteratively follows a path in where Ax_i-b difference decreases fastest. Since the gradient of a function shows the direction of its greatest growth, η_x gradient is negatively iterated. η_x function's negative gradient is the difference of the original value b and is approximation Ax. Steep descent algorithm starts from a random x_0, and takes the error difference that occurs when x_i is placed in equation, r_i, and multiplies it with a weighting factor α.

The steepest descent method can iterate steps in the same direction and this can lengthen the convergence time. Conjugate gradient method is an advanced form of steepest descent method, and in this method the adjacent steps are taken perpendicular to each other, which speeds up the convergence. If p_i and p_{i+1} are two adjacent search directions, these must be perpendicular in the conjugate gradient method.

A new direction is found using the previous direction and the error difference. A second weight factor β is defined in the conjugate gradient and is used to determine the direction of the iteration. An iterative solution, $x_{i+1,}$ can be found with conjugate gradient method as,

$$x_{i+1} = x_i + \alpha_i p_i. \qquad (2.7)$$

The error difference in the next step, r_{i+1} is then calculated as,

$$r_{i+1} = r_i - \alpha_i A p_i. \qquad (2.8)$$

In conjugate gradient method, an acceptable solution can be determined by confirming that with each iteration, the error difference approaches to a minimum. If the difference begins to increase or two adjacent iterations has an error difference of more than 15%-20%, then the iterations are ceased, and it is assumed that the closes solution to the Ax=b function has been found [37].

3. MATERIALS AND METHODS

3.1   SIMULATIONS

3.1.1   Data Preparation

A volunteer was scanned with a 3T MR scanner (Philips Medical Systems, Best, Netherlands) using a ^{31}P surface coil. A disc at the center of this coil that contained both water and methylphosphonic acid, was used for localization.   Anatomical brain images were acquired using a body coil and turbo field echo sequence (TFE) (TR=75ms, TE=5ms, flip angle (FA) =30°). Using image selected in vivo spectroscopy (ISIS), a ^{31}P MR spectrum was acquired (TR=5s, 128 signal averages, 3000Hz, idle period=0.333ms, 1024 time points, 27cc voxel size, scan time=11min). After this spectrum was processed with a 10Hz Gaussian filter, phase correction, baseline removal, and measurements were done using AMARES under jMRUI [38]. Amplitude (a) and frequency (f) values were calculated for each peak using AMARES, and were used to form a healthy spectrum in the time domain with the following equation, using MATLAB (The Mathworks Inc., Natick, MA),

$$y_n = \sum_k a_k e^{-(d_k + i2\pi f_k)t_n}, \tag{3.1}$$

and for all peaks a d_k=30Hz was used. A tumor spectrum was simulated using the same method. Peak ratios of the tumor spectrum and healthy spectrum for the metabolites PCr, γ-ATP, α-ATP, β-ATP, GPC, GPE, Pi, PC and PE, were given as 0.49, 1.0, 1.0, 1.0, 2.16, 1.86, 1.47, 2.06, 2.63, respectively. Noise was added to each spectrum. In Figure 3.1 and 3.2, simulations for healthy and tumor ^{31}P-MR spectra can be seen. Using healthy and tumor spectra, two dimensional 8x8, 16x16 and 32x32 ^{31}P-MRSI datasets were created, where the upper left corner contained tumor and the remaining voxels had healthy spectra. (Figure 3.3)
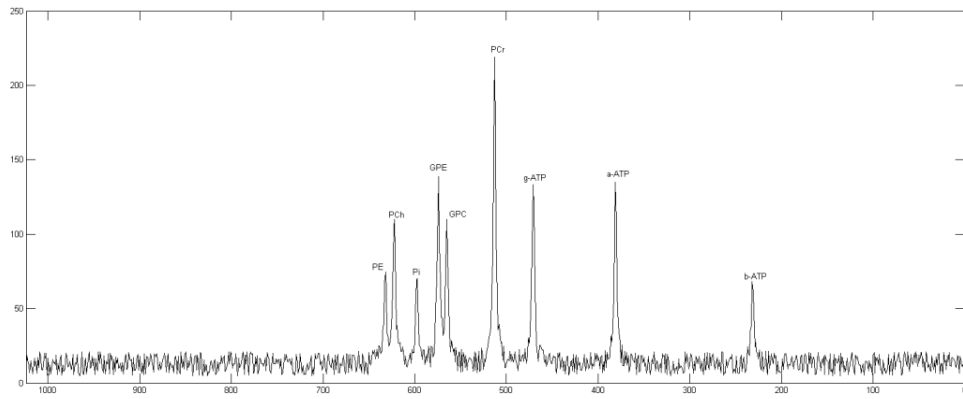
Figure 3.1 ^{31}P- MR spectrum simulation of healthy brain tissue.
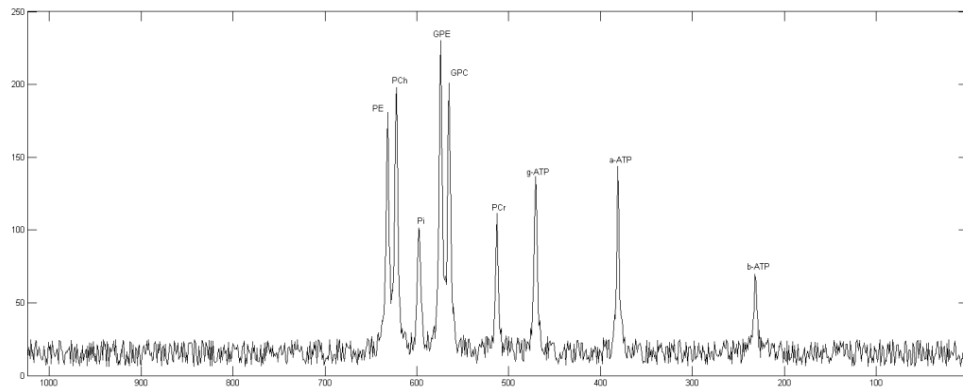
Figure 3.2 ^{31}P- MR spectrum simulation of a brain tumor.
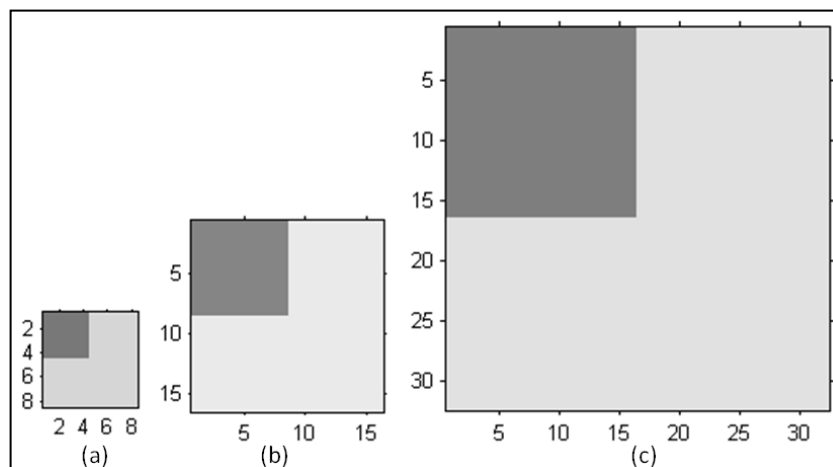
Figure 3.3 PCr peak intensity across the 2D **(a)** 8x8 **(b)** 16x16 **(c)** 32x32 ^{31}P-MRSI datasets containing tumor (dark), and healthy (light) regions.

The compressed sensing method requires the Fourier transform results of the solution to be similar with the original data, as well as the signal formed to be sparse enough to be compressed with Wavelet transform [33]. Due to the nature of the compressed sensing, the data has to be randomly undersampled in the Fourier space. Therefore, k-space data of the simulated dataset was randomly undersampled using various undersampling patterns. An image in the Fourier space has the low frequency information in the middle portion, where the main definition of the image is found. Outer portion of k-space has the high frequency data (details of the image), therefore in order to avoid loss of data when undersampling, mask had to be designed such that it would take the information at the central portion of the k-space. Fully random undersampling mask and random undersampling masks that preserved center of the k-space, were created, where acquired data points were set to 1 and unacquired ones were 0. Figure 3.4, 3.5, and 3.6 show fully random undersampling and center preserved random undersampling masks.

^{31}P-MRSI datasets which were simulated in 8x8, 16x16, and 32x32 matrices were multiplied with these random masks, and after that the data were reconstructed using compressed sensing algorithm.
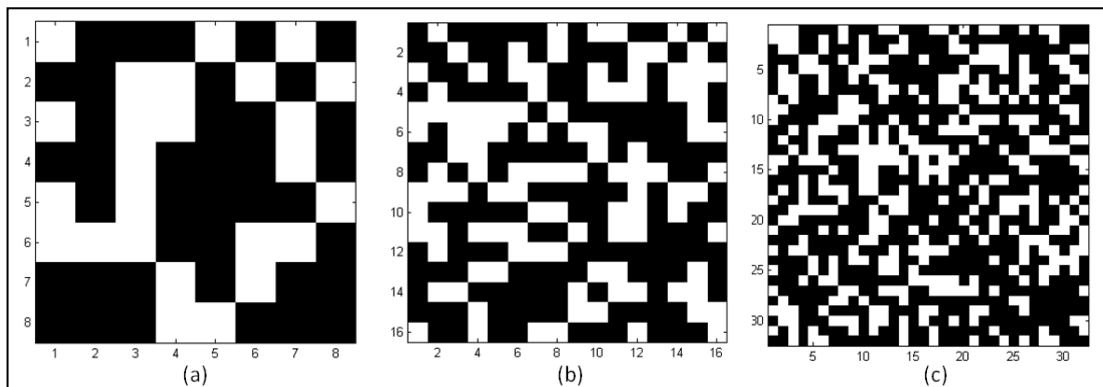
Figure 3.4 Fully random undersampling patterns for **(a)** 8x8, **(b)** 16x16 and **(c)** 32x32 arrays.
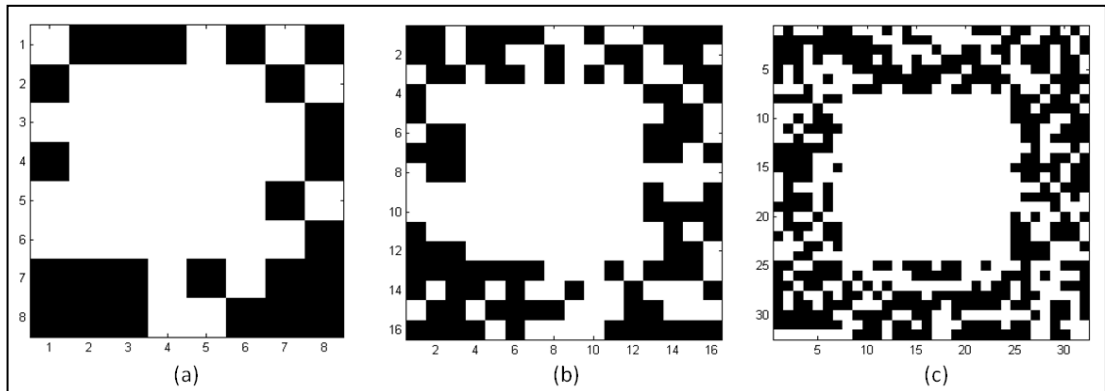
Figure 3.5 Random undersampling patterns with preserved k-space center zone and **(a)** R=1.6 for 8x8, **(b)** R=1.64 for 16x16 and **(c)** R=1.67 for 32x32 arrays.
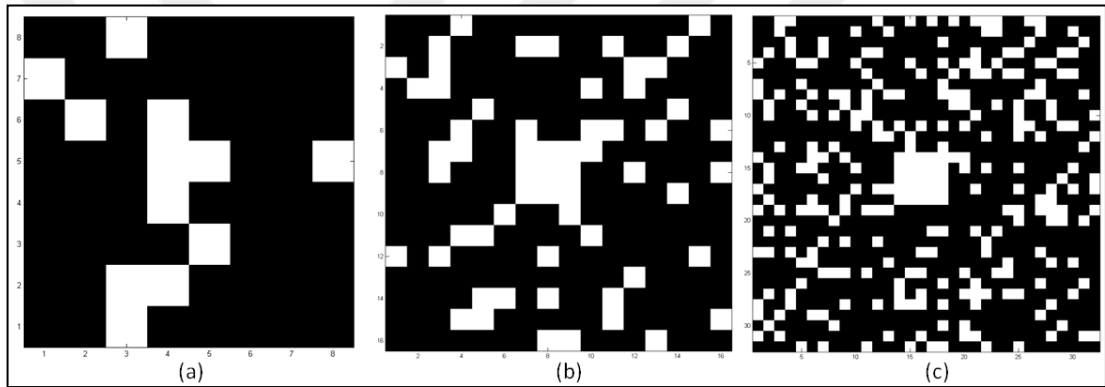
Figure 3.6 Random undersampling patterns with preserved k-space center zone and **(a)** R=5.33 for 8x8, **(b)** R=4.26 for 16x16 and **(c)** R=3.71 for 32x32 arrays.

3.1.2   2D Iterative Frame Based Compressed Sensing Reconstruction

SparseMRI software package that was designed for compressed sensing method was modified for reconstruction of ^{31}P MR spectroscopic datasets. Resultant randomly undersampled k-space data was reconstructed using this software. Undersampled datasets were inverse Fourier transformed along k_y first, and k_x-k_f data was reconstructed for each y point, using SparseMRI software package [39]. Obtained datasets were inverse Fourier transformed along k_x and k_y-k_f data was reconstructed for each x point. L$_1$-norm and total variation weights were chosen as 0.001, empirically. 2D Length-4 Daubechies Wavelet transform was used as the sparsifying transform.

3.1.3   3D Direct Compressed Sensing Reconstruction

3D direct compressed sensing reconstruction is an improved algorithm of Sparse MRI (2D iterative frame based) for faster ^{31}P-MRSI [40]. In 2D iterative frame based reconstruction, undersampled ^{31}P-MR spectroscopic data was reconstructed iteratively, due to the main and sub-functions of Sparse MRI being 2D. This algorithm was scrutinized, and relevant functions were determined. Required changes in the algorithm were implemented to adapt the routines for 3D direct reconstruction. A third dimension was added to the undersampling masks. The zero padding function of Sparse MRI that takes only central part of frequency was converted from 2D to 3D. In this function, 6x6 Hamming window was created, and it was placed at the center of the zero matrix which was created as the same size with ^{31}P MR dataset. In 3D direct compressed sensing, a 3D Hamming window was created, and it was placed at the center of 3D zero matrix, to obtain the central frequency information of k_x-k_y-k_f data. After the acquisition of central frequency information, phase was calculated and verified. A Fourier operator was created and the data was scaled. In Sparse MRI software package, the sampling and scaling works were done in two dimensional, consequently these functions were modified for 3D data reconstruction. The scaled dataset was multiplied with Wavelet operator and reconstructed with compressed sensing algorithm. For the Wavelet operator, a length-4 Daubechies was used. The dimensions of the operator and the data, should agree for multiplication, therefore, multiplication algorithms used to create the Wavelet operator were converted from 2D to 3D. Resultant 3D algorithm was designed to work on multi-slice ^{31}P-MR spectroscopic datasets in each iteration.

3.2   PARADISE

Paradise is a software that can simulate a Philips MR scanner with all of its aspects, and has all the system software codes of the corresponding MR scanner built in. Every MR system vendor has their own software, and usually their software written in complex C codes. Philips MR system software is written in GOAL-C, which is a programming language that resembles C. This software consists of numerous header files and source codes. Spectroscopic data acquisition system codes were inspected, relevant functions and required modifications were determined in these header files, and source codes. Compressed sensing options and effects of undersampling mask were added to where MR

spectroscopic data acquisition was done. Several parameters were added to be shown at the user interface of MR scanner. 8x8 and 16x16 undersampling masks which were chosen according to the simulation results, were transferred in an appropriate format into the software to be used within Philips MR scanner. Data acquisition direction and format of Philips MR scanner were identified, and an appropriate code was written for the masks to be applied properly for the data acquisition. The software normally automatically fills unacquired k-space points with zeros and Fourier transforms data before exporting it. The part of the pulse sequence that disables the reconstruction was determined, and 'EX_SPY_kspace_data' parameter was added to be able to interfere from user interface of MR scanner. k-space points are required for compressed sensing reconstruction algorithm to be used and with this modification raw data was obtained from the system. The user interface after the activation of additional code modifications can be seen in Figure 3.7.
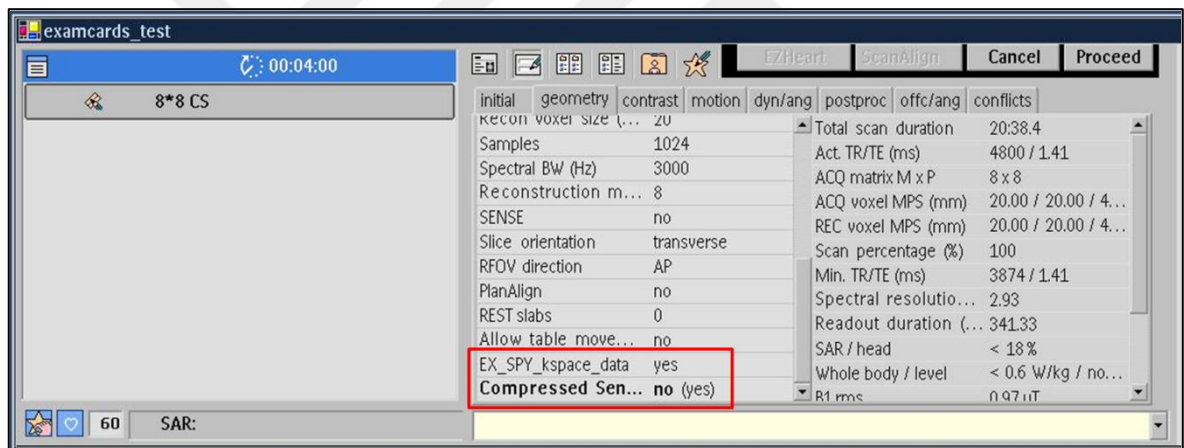
Figure 3.7 The screenshot of the modified user interface of MR scanner (compressed sensing disabled in this shot).

3.3 DATA ACQUISITION

A 3T MR scanner (Philips Medical Systems, Best, Netherlands), and a dual channel ^{31}P/^{1}H volume cranial coil was used to acquire ^{31}P-MR spectra with pulse and acquire (PA) technique (TR=4.8s, NA=4, 3000Hz, 1024 points, field of view (FOV)=160x160mm, 20x20x40mm voxel size, scan time=16 min). Datasets were obtained from a healthy volunteer and a brain tumor patient.

3.4 DATA PROCESSING

^{31}P MR spectroscopic full datasets were processed using jMRUI software. In order to filter out the noise, two consecutive 10Hz Lorentzian filters were used to apodize the signal. jMRUI was used to overlay the DICOM images with the spectrum of each voxel, and this was used to determine the healthy and tumorous regions. In order to read the dataset in a format that complies with the Philips ^{31}P MR spectroscopic imaging standards, existing reader scripts for MATLAB (The Mathworks Inc., Natick, MA), were used and modified accordingly. Data read by MATLAB, was analyzed using ppm ranges of the metabolites, PCr, γ-ATP, α-ATP, β-ATP, GPC, GPE, Pi, PE, PC. Peak heights and ratios taken from healthy and tumorous regions were analyzed.

^{31}P MR spectroscopic undersampled datasets were read in MATLAB, and domain of datasets were changed into k-space for 3D direct reconstruction. The datasets of a volunteer and a brain tumor patient were reconstructed using 3D direct compressed sensing algorithm. The reconstructed datasets were written in a format that complies with Philips ^{31}P MR spectroscopic imaging standards using MATLAB, to compare the full and reconstructed ^{31}P MR spectra. The reconstructed datasets were apodized with two consecutive 10 Hz Lorentzian filters to reduce the noise, and filtered datasets were read by MATLAB to analyze the difference between original and reconstructed ^{31}P MR spectra.

3.5 DATA ANALYSIS

3.5.1 Bland Altman Method

A Bland Altman statistical test was used to detect a significant difference between mean metabolite peak ratios of the original, 2D iterative frame based and 3D direct compressed sensing datasets within the tumor and healthy regions. Bland-Altman method compares the results of two different applications under same or similar parameters, over a range of different parameter pairs, and each method having an error margin of their own. For *n* samples, *2n* total assessments are done by using the two methods to be evaluated. Sample pairs are actually derived from the same sample in the original dataset, but evaluated with two different methods. A Cartesian coordinate system is formed as a result of Bland-

Altman method. One point in the Cartesian space is assigned for each sample, where x-axis value is the mean of the relevant pair, and y-axis value is the difference between the relevant pair.

3.5.2 Wilcoxon Rank Sum Test

A rank sum test was utilized to see if the SNR of PCr, Pi, and β-ATP, and Pi/PCr, PCr/β-ATP, and PCr/PE metabolite ratios in the original, 2D iterative frame based, and 3D direct compressed sensing reconstructed datasets were significantly different between the tumor and healthy regions. Wilcoxon rank sum test is a more powerful nonparametric alternative to the commonly used unpaired t-test. It tests whether two different populations have significantly different characteristics for a given parameter.

3.5.3 Bonferroni Correction

Bonferroni correction was applied, and $p < 0.005$ was considered to be significant. It is used with multiple comparison tests. The familywise error rate is calculated and therefore the tests overall precision is improved.

3.5.4 Root Mean Square Error

Root mean square error (RMSE) was calculated for quantification of the error of reconstruction techniques. RMSE can be formulated as,

$$\text{RMSE} = \sqrt{\frac{\sum_{i=1}^{n}\left(X_{O,i} - X_{E,i}\right)^2}{n}} \tag{3.2}$$

where X_O is the observed value, X_E is the expected value, and n is the total number of points in dataset. In this study, original dataset was used as observed, and 2D and 3D reconstructed compressed sensing datasets were used as expected values.

4. RESULTS

4.1   2D Iterative Frame Based Compressed Sensing Reconstruction

The amount of distortion in the 2D image at a certain frequency and more importantly loss of data in simulated ^{31}P-MR spectra were assessed when fully random undersampling patterns were used. In Figure 4.1, 2D image outputs of fully random undersampled reconstruction for 8x8, 16x16, and 32x32 voxels are shown. Tumor region in left upper portion could not be distinguished. Similarly, intense distortion, signal loss and phase errors were observed in reconstructed ^{31}P-MR spectra of all sizes (Figure 4.2, 4.3, 4.4). In simulations, substantial distortion is expected in the reconstructed images and spectra when the center of the k-space is not sampled, and our observations have confirmed this.
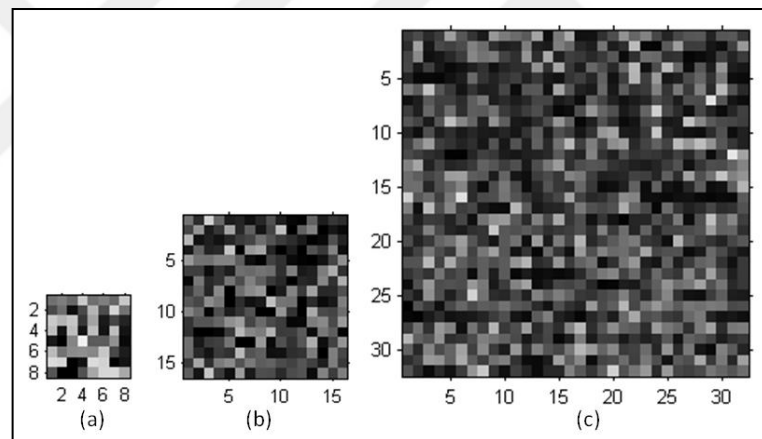
Figure 4.1 2D PCr image outputs of **(a)** 8x8, **(b)** 16x16, and **(c)** 32x32 arrays for 2D iterative frame based reconstruction which was undersampled with a fully random mask.
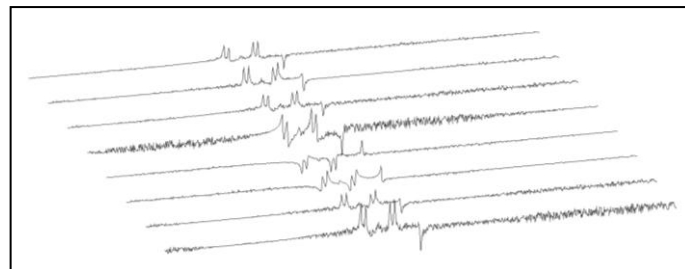
Figure 4.2 A column of 2D iteratively reconstructed 8x8 ^{31}P-MR spectra which was undersampled with fully random mask.
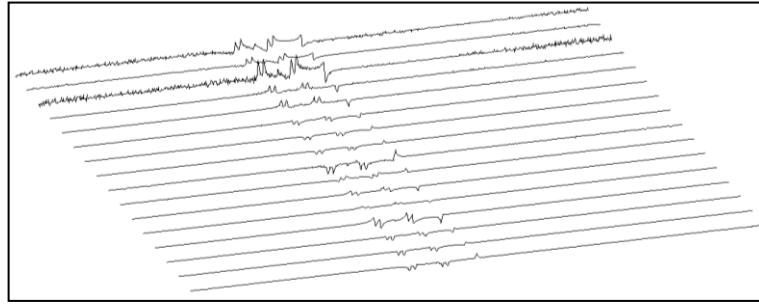
Figure 4.3 A column of 2D iteratively reconstructed 16x16 ^{31}P-MR spectra which was undersampled with fully random mask.
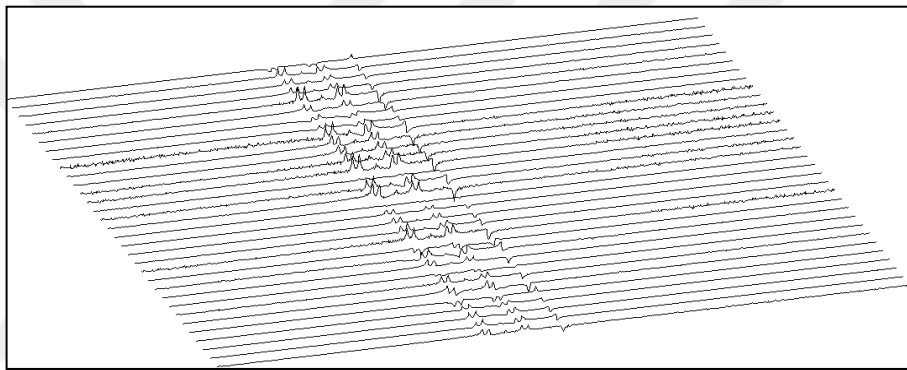
Figure 4.4 A column of 2D iteratively reconstructed 32x32 ^{31}P-MR spectra which was undersampled with fully random mask.

^{31}P-MR spectroscopic datasets were undersampled with a mask that preserved k-space center zone and their reduction factors were 1.6, 1.64, and 1.67 for 8x8, 16x16 and 32x32 respectively. The resultant PCr frequency images of random undersampled with preserved k-space center zone reconstruction for all sizes can be seen in Figure 4.5. In these images, tumor region can be differentiated more clearly. Likewise, tumor and healthy regions were separable in ^{31}P-MR spectral data for all sizes (Figure 4.6, 4.7, 4.8). Both 2D images and spectra of reconstructed ^{31}P-MR spectroscopic data that was undersampled with center preserved mask, were observed to be better due to the fact that main information of data exist on the central portion of the Fourier domain.

Figure 4.5 2D PCr image outputs of **(a)** 8x8, **(b)** 16x16, and **(c)** 32x32 arrays for 2D iterative frame based reconstruction which was undersampled with a center preserved random mask.
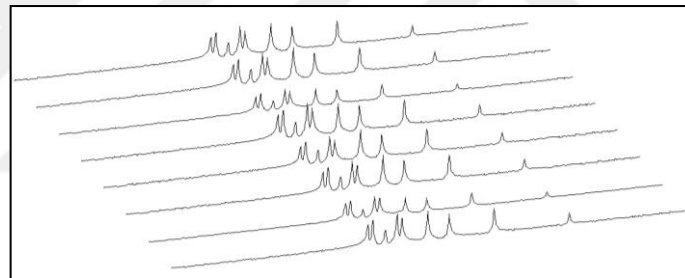
Figure 4.6 A column of 2D iteratively reconstructed 8x8 ^{31}P-MR spectra which was undersampled with a center preserved random mask.
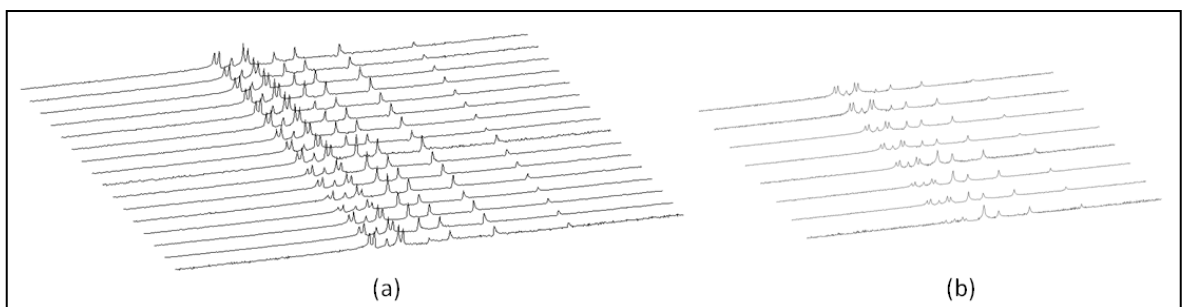
Figure 4.7 A column of 2D iteratively reconstructed **(a)** 16x16 and **(b)** its central 8x8 ^{31}P-MR spectra which was undersampled with a center preserved random mask.
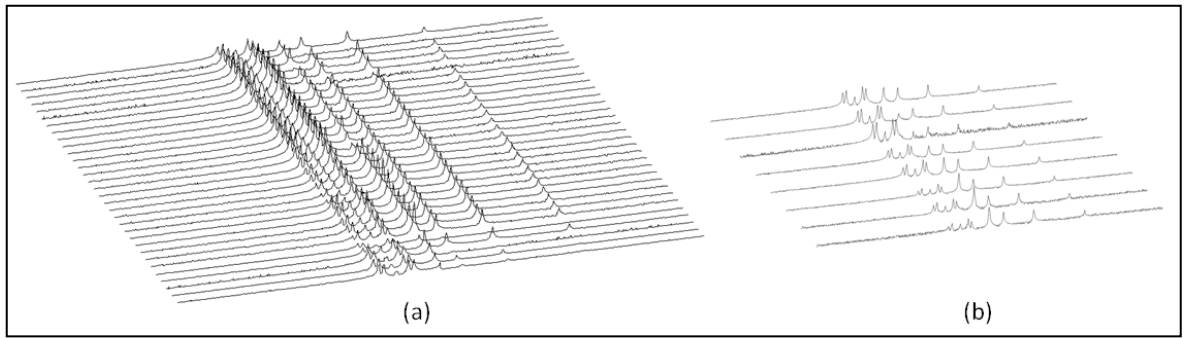
Figure 4.8 A column of 2D iteratively reconstructed **(a)** 32x32 and **(b)** its central 8x8 ^{31}P-MR spectra which was undersampled with center preserved random mask.

In Figure 4.9, the ^{31}P-MR spectra of 8 voxels acquired from healthy and tumor regions using original and compressed sensing data are shown. Upper 4 voxels are tumor and lower 4 voxels are healthy spectra. In both of the datasets, tumor and healthy spectral regions are distinguished with ease.
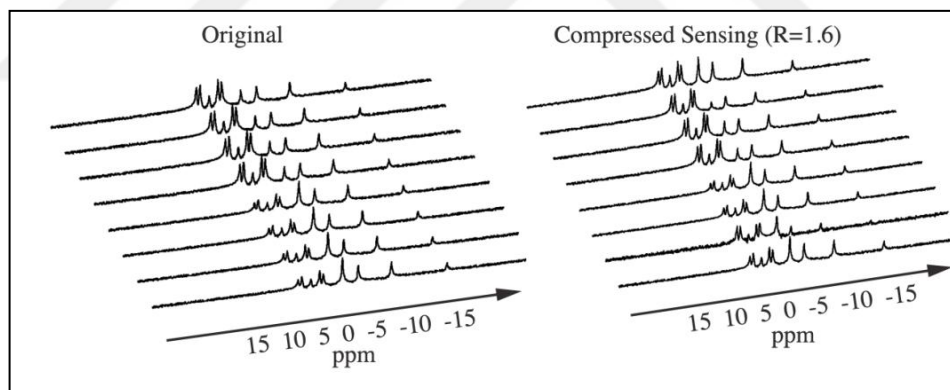
Figure 4.9 Eight voxels showing the transition between the healthy and tumor voxels for the original and 2D iteratively reconstructed compressed sensing datasets.

4.2 3D Direct Compressed Sensing Reconstruction

^{31}P-MR spectroscopic datasets were undersampled with a mask that preserved the 25% of k-space along x and y directions, and 7.5% of central part. 7.5% central portion was chosen empirically to obtain approximate solution with higher reduction factor. For even shorter acquisition times, the reduction factors used for 3D direct reconstruction were higher than 2D iterative frame based reconstruction. 2D PCr image outputs of 3D direct reconstruction

for all sizes can be seen in Figure 4.10. Although datasets were undersampled with higher reduction factor, tumor and healthy regions were separated clearly in 3D directly reconstructed images. Likewise, 3D directly reconstructed and original ^{31}P-MR spectra were very similar. In figures 4.11, 4.12, and 4.13, 3D directly reconstructed ^{31}P-MR spectroscopic datasets are shown for all sizes.
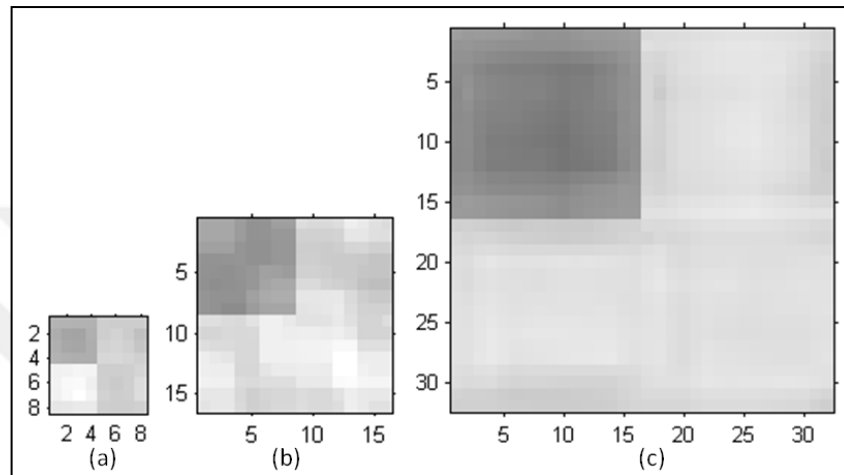
Figure 4.10 2D PCr image outputs of **(a)** 8x8, **(b)** 16x16, and **(c)** 32x32 arrays for 3D direct reconstruction.
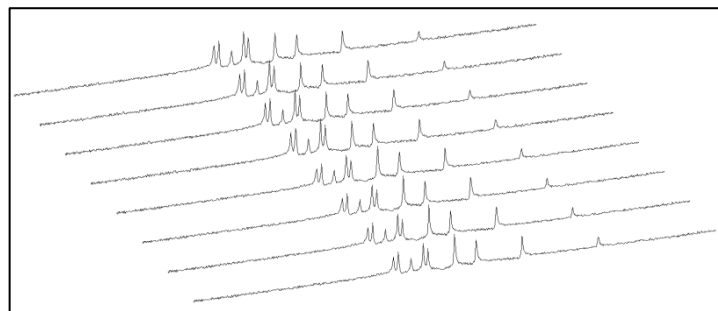
Figure 4.11 A column of 3D directly reconstructed 8x8 ^{31}P-MR spectra.
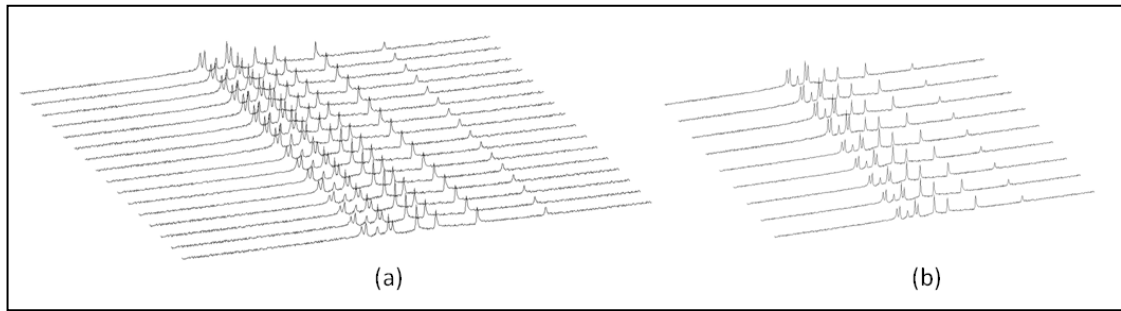
Figure 4.12 A column of 3D directly reconstructed **(a)** 16x16 and **(b)** its central 8x8 ^{31}P-MR spectra.
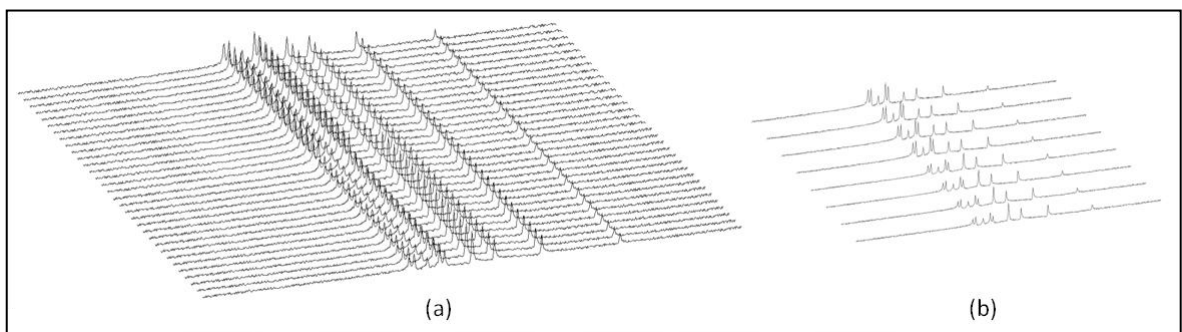
Figure 4.13 A column of 3D directly reconstructed **(a)** 32x32 and **(b)** its central 8x8 ^{31}P-MR spectra.

The ^{31}P-MR spectra of 8 voxels acquired from healthy and tumor regions using original and 3D directly compressed sensing data were shown in Figure 4.14. In original and 3D directly compressed sensing datasets, tumor and healthy spectral regions can be easily separated from each other.
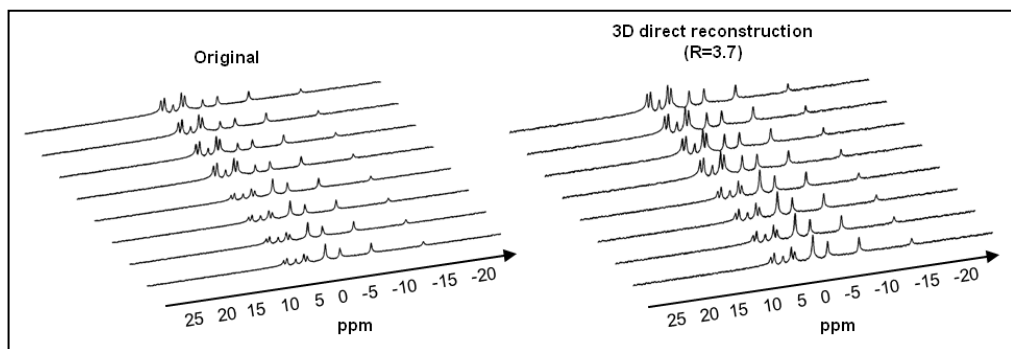
Figure 4.14 Eight voxels showing the transition between the healthy and tumor voxels for the original and 3D directly reconstructed compressed sensing datasets.

4.3 Comparison of 2D Iterative Frame Based and 3D Direct Compressed Sensing Reconstruction

The random undersampling patterns preserved the 7.5% of central part while reducing the k-space data by a reduction factor of 4.26 for 16x16, and 3.71 for 32x32 arrays. For 8x8 datasets, the undersampling pattern which contained the 40% of whole data and preserves the 10% of center was used, so that it would be possible to compare 2D iterative frame based and 3D direct CS reconstruction algorithms (Figure 4.15). The acquisition times of original and undersampled (U) datasets are given in Table 4.1. Even though the acquisition time of ^{31}P-MR spectroscopic imaging would decrease substantially, time required for 32x32 acquisition would still not feasible for clinical applications.
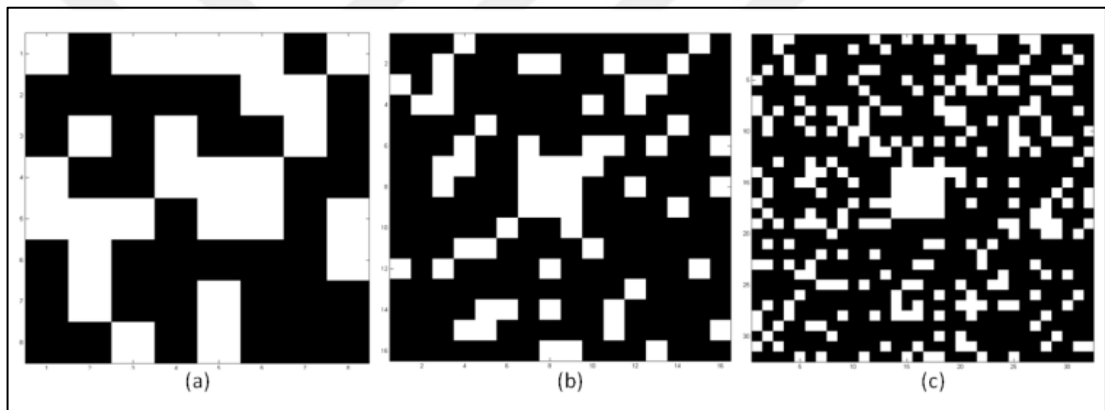
Figure 4.15 Random undersampling patterns with preserved k-space center zone and **(a)** R=2.37 for 8x8, **(b)** R=4.26 for 16x16 and **(c)** R=3.71 for 32x32 arrays

Table 4.1 Comparison of acquisition times.

Size	O	U
8x8	5.3 min	2.25 min
16x16	21 min	5 min
32x32	85.3 min	23 min

PCr images of 2D iteratively reconstructed datasets can be seen in Figure 4.16. Tumor region could not be distinguished from the healthy region. Tumor region was easily distinguished from the healthy region in 2D images of 3D directly reconstructed datasets, unlike 2D iteratively datasets (Figure 4.17).
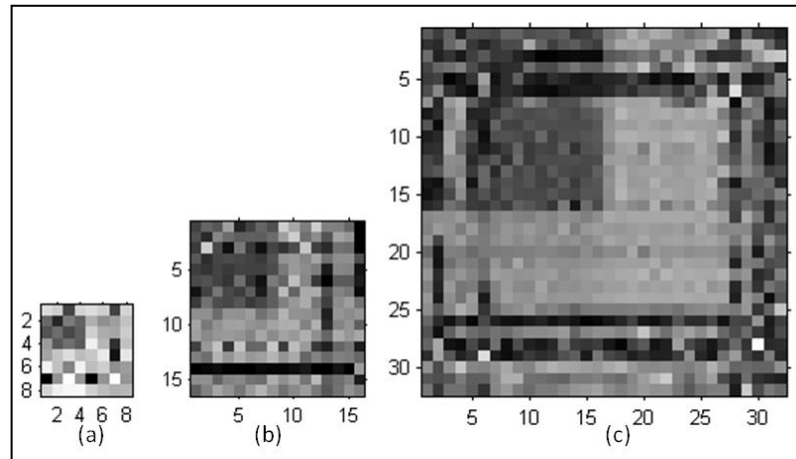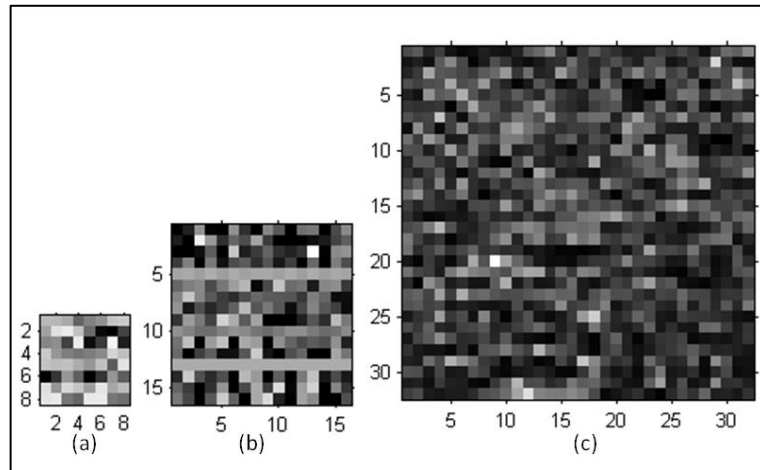
Figure 4.16 2D PCr image outputs of **(a)** 8x8, **(b)** 16x16, and **(c)** 32x32 arrays for 2D iterative frame based reconstruction which was undersampled with 2.37, 4.26, and 3.71 reduction factors, respectively.
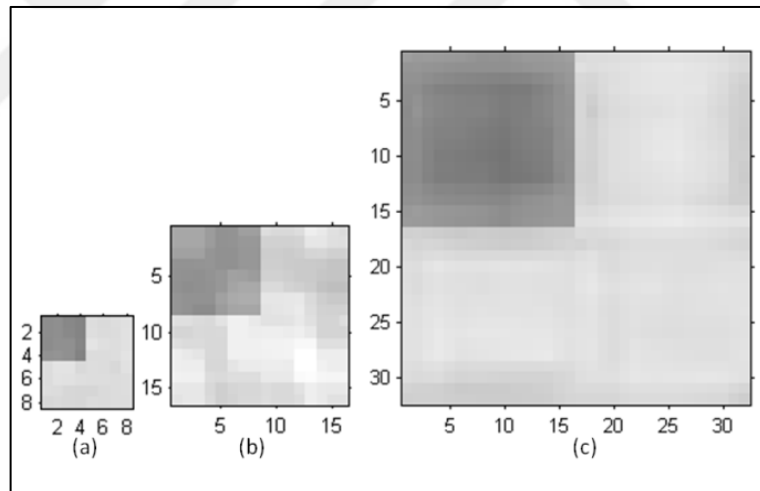

Figure 4.17 2D PCr image outputs of **(a)** 8x8, **(b)** 16x16, and **(c)** 32x32 arrays for 3D direct reconstruction which was undersampled with 2.37, 4.26, and 3.71 reduction factors, respectively.

A 16x16 voxel reconstructed PCr images, and their middle 4x4 spectra are shown in figures 4.18, and 4.19. When 2D iterative frame based CS reconstruction was used, tumor and healthy regions were not separable, while 3D direct CS reconstruction resulted in an image and spectra where tumor and healthy regions were clearly separable.
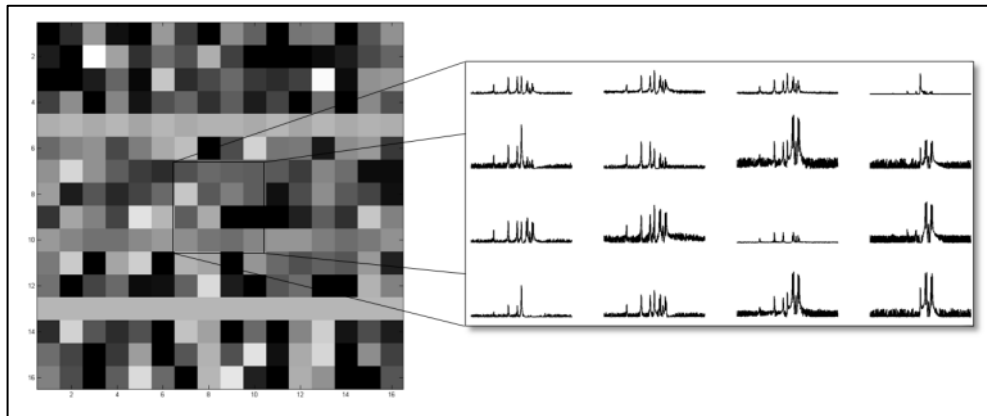
Figure 4.18 A 2D iteratively reconstructed 16x16 image and spectra of central 4x4.
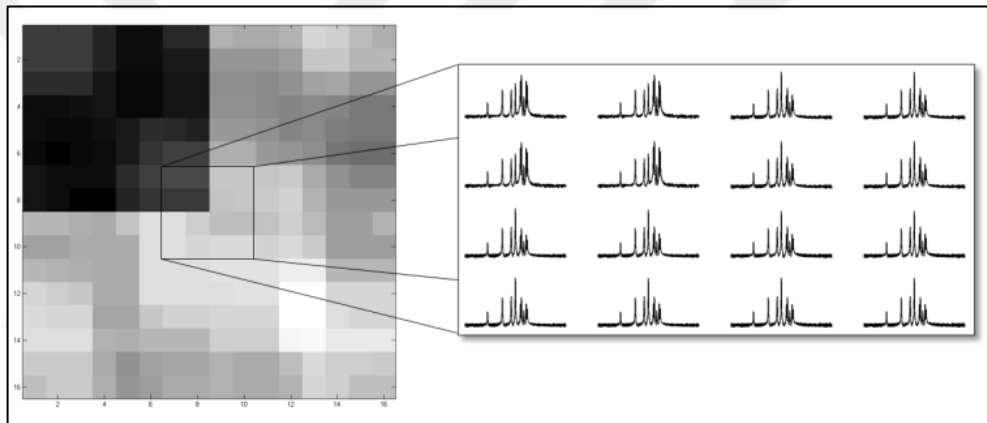
Figure 4.19 A 3D directly reconstructed 16x16 image and spectra of central 4x4.

The middle 8 voxels of ^{31}P-MR spectra of 32x32 original, 2D iterative frame based, and 3D direct CS reconstruction datasets are shown in Figure 4.20. Top four voxels were tumor, and the rest were healthy spectra. In original and 3D directly reconstructed datasets, tumor and healthy regions were differentiable, when several voxel distortions, and signal losses were observed in spectra of 2D iteratively reconstructed datasets.
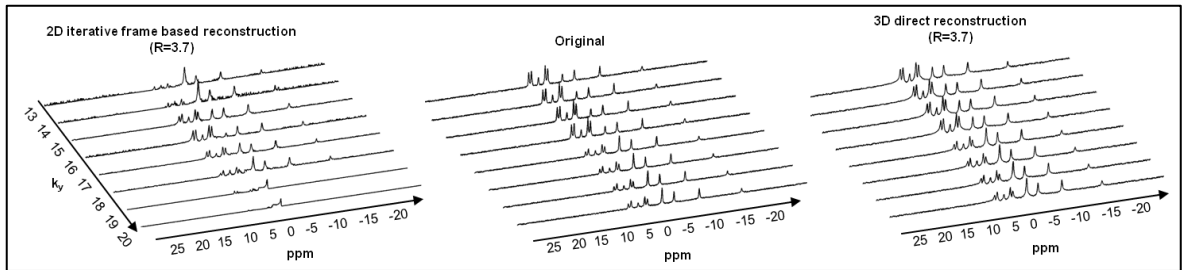
Figure 4.20 Eight voxels showing the transition between the healthy (bottom four) and tumor (top four) voxels for the original and 2D and 3D reconstructed CS datasets.

Metabolite ratios in tumor and healthy regions of original, 2D iteratively, and 3D directly reconstructed CS datasets are given in Table 4.2. Rank sum test results indicated that ratio differences between tumor and healthy peaks were statistically significant for 3D direct CS reconstruction and original datasets, while 2D iterative frame based CS reconstruction datasets peak ratio differences were not significant (p<0.005).

Table 4.2 Pi/PCr, PCr/β-ATP, and PCr/PE metabolite ratios in tumor and healthy regions of the original, 2D iteratively, and 3D directly reconstructed compressed sensing datasets for all sizes.

Size		Tumor			Healthy		
		Pi/PCr	PCr/β-ATP	PCr/PE	Pi/PCr	PCr/β-ATP	PCr/PE
	Original	0.9±0.0	1.6±0.0	0.7±0.0	0.3±0.0	3.04±0.0	2.7±0.0
8x8	2D CS	0.46±0.28	4.56±3.87	2.05±1.74	3.78±12.92	5.54±12.1	1.52±1.2
	3D CS	0.88±0.04	1.98±0.1	0.7±0.03	0.4±0.01	3.04±0.1	2.3±0.1
16x16	2D CS	29.3±113	13.6±54	33.8±120	52.8±154.8	4.7±6.2	43.6±167
	3D CS	0.72±0.04	1.9±0.1	0.9±0.1	0.36±0.03	2.97±0.15	2.7±0.5
32x32	2D CS	0.45±0.54	26.9±85.9	58.3±205	0.59±0.98	25.4±78.2	53±148.5
	3D CS	0.86±0.09	1.7±0.2	0.7±0.1	0.34±0.0	2.7±0.05	2.4±0.1

In Table 4.3, tumor over healthy ratios of mean metabolite peaks for original, 2D iterative frame based, and 3D direct CS reconstruction datasets are given. Although the mean metabolite peak values were similar between original and 3D direct CS reconstruction datasets, they were not similar for 2D CS reconstruction datasets.

Table 4.3 Tumor over healthy ratios of mean PCr, Pi, and β-ATP peak heights of original, 2D iteratively and 3D directly reconstructed compressed sensing (CS) datasets for all sizes.

Tumor/Healthy Ratio of Mean Metabolite Peak		PCr	Pi	β-ATP
Original		0.56	1.44	1.02
8x8	2D CS	1.1	0.88	0.9
	3D CS	0.6	1.48	0.97
16x16	2D CS	1.01	0.88	0.86
	3D CS	0.67	1.33	1.06
32x32	2D CS	1.23	1.06	1.12
	3D CS	0.58	1.43	0.89

Bland Altman test results of original and 2D iterative frame based CS, and original and 3D direct CS reconstruction can be seen in Table 4.4. Pi/PCr, PCr/β-ATP, and PCr/PE ratios of 3D direct reconstruction and original were found to have very close values, resulting in a small standard deviation that resulted in few outliers. Bias and standard deviation of all ratios for 2D reconstructed CS dataset were found to be high.

Table 4.4 Bland Altman test results for the number of outliers, bias and std(bias) for the similarity of the peak ratios the original and 2D and 3D reconstructed compressed sensing datasets.

Bland Altman Test Results (16x16)		2D Iterative Frame Based Reconstruction			3D Direct Reconstruction		
		Pi/PCr	PCr/β-ATP	PCr/PE	Pi/PCr	PCr/β-ATP	PCr/PE
T	#outliers	4	2	3	0	1	2
	mean(diff)	29.3	12.6	33.4	0.1	0.3	0.2
	std(diff)	112.7	54.1	120.3	0.04	0.1	0.09
H	#outliers	4	3	3	0	4	4
	mean(diff)	52.6	3.7	43.6	0.02	0.1	0.4
	std(diff)	154.7	5.3	166.7	0.02	0.1	0.3

Effect of the noise level on 2D and 3D CS reconstructions were, found by calculating RMSE, which can be seen in Table 4.5. While the effect of the increase in noise level on RMSE value of recon datasets is apparent, RMSE values were still lower for 3D CS datasets. RMSE values of 3D CS datasets that were undersampled with various different patterns that have different central k-space percentages and total k-space points can be seen in Table 4.6. Since it is necessary to preserve k-space center for better reconstruction, lower sampling in this central portion was directly related to the quality of the signal, and

increased the RMSE value. By evaluating the number of points, it was seen that the RMSE increase in 8x8 was greater than the increase in 16x16.

Table 4.5 Root mean square error (RMSE) values of 2D iteratively and 3D directly reconstructed CS datasets with different noise levels.

RMSE		2D CS			3D CS		
		8x8	16x16	32x32	8x8	16x16	32x32
Noise level*	8%	7.9×10^{-3}	9.8×10^{-3}	1.1×10^{-2}	9.1×10^{-4}	1.4×10^{-3}	1.3×10^{-3}
	30%	1.1×10^{-2}	1.6×10^{-2}	1.5×10^{-2}	1.1×10^{-3}	1.7×10^{-3}	1.4×10^{-3}
	40%	1.4×10^{-2}	1.8×10^{-2}	1.9×10^{-2}	1.2×10^{-3}	2.1×10^{-3}	1.4×10^{-3}
	50%	1.4×10^{-2}	1.8×10^{-2}	2.4×10^{-2}	1.6×10^{-3}	2.2×10^{-3}	2.1×10^{-3}

*The standard deviation of the additional noise was set as the percentage of the maximum peak intensity within the spectrum.

Table 4.6 RMSE values of 3D directly reconstructed CS datasets with using different undersampling patterns.

RMSE		Percentage of the central k-space points sampled (16x16)			Percentage of the central k-space points sampled (8x8)		
		7.5%	6.5%	5.5%	7.5%	6.5%	5.5%
Percentage of the total k-space points sampled	10%	2.2×10^{-3}	2.6×10^{-3}	1.8×10^{-2}	1.3×10^{-2}	1.5×10^{-2}	1.6×10^{-2}
	20%	1.9×10^{-3}	1.9×10^{-3}	4.5×10^{-3}	3.7×10^{-3}	1.5×10^{-2}	1.6×10^{-2}
	25%	9.1×10^{-4}	1.3×10^{-3}	3.9×10^{-3}	3.2×10^{-3}	3.6×10^{-3}	1.5×10^{-2}

4.4   Compressed Sensing Reconstruction for Accelerated ^{31}P-MR Spectroscopic Imaging of Human Brain

User interface of Philips MR scanner is shown in Figure 4.21, when PA pulse sequence was used, compressed sensing (Compressed Sensing=no) option was disabled, and reconstruction (EX_SPY_kspace_data=yes) option was enabled. The scan time was 20:38 min for 8x8 full data acquisition. When compressed sensing (Compressed Sensing=yes) option and raw data acquisition were enabled (EX_SPY_kspace_data=no), the scan time was reduced to 4 min (Figure 4.22), and 12 k-space points that belonged to the desired undersampling pattern, was acquired with a reduction factor of 5.33 (Figure 4.23).
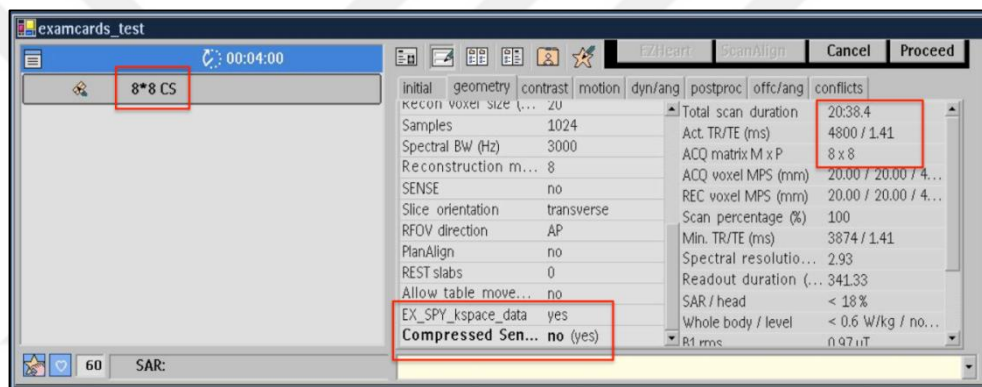
Figure 4.21 The screenshot of Philips MR scanner user interface. The scan time was 20:38 min when compressed sensing option was disabled, and the reconstruction option (EX_SPY_kspace_data) was enabled.
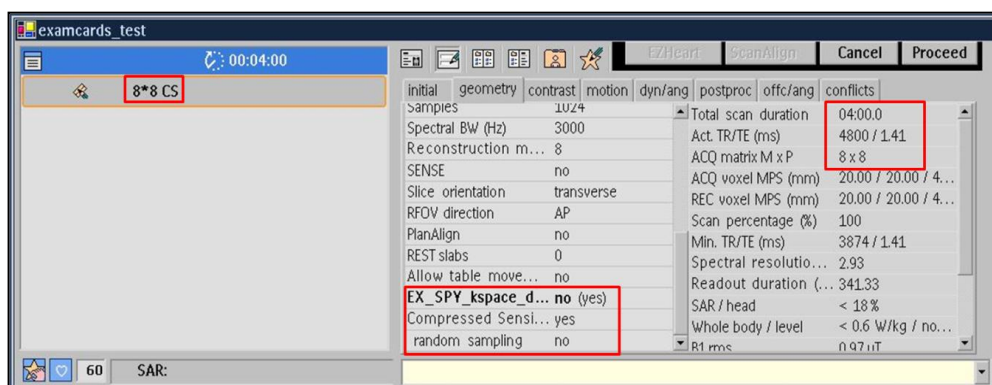
Figure 4.22 The screenshot of Philips MR scanner user interface. The scan time was reduced to 4 min when compressed sensing option was enabled, and the reconstruction option was disabled.
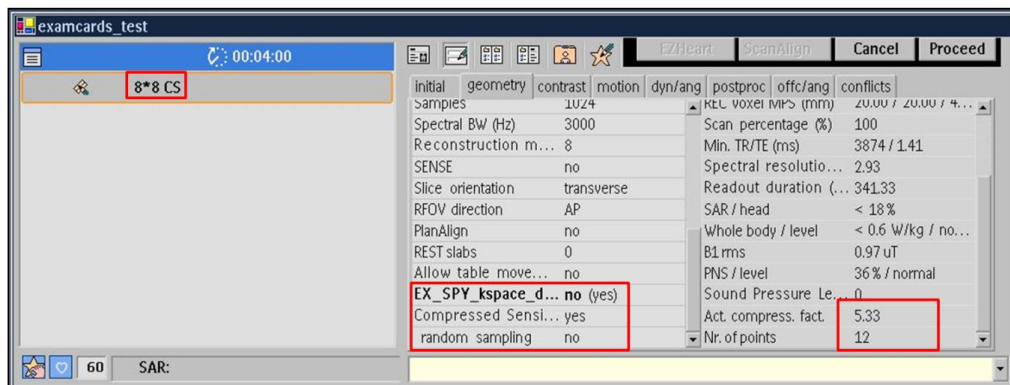
Figure 4.23 The screenshot of Philips MR scanner user interface. 12 k-space points that belonged to the undersampling pattern, was acquired with a reduction factor of 5.33 when compressed sensing option was enabled, and the reconstruction option was disabled.

In Figure 4.24, ^{31}P-MR spectroscopic FID data of a volunteer which was acquired with compressed sensing, is shown. Data acquisition was done in k-space at where undersampling mask had non-zero elements. This data was processed with compressed sensing reconstruction algorithm to obtain spectral data.
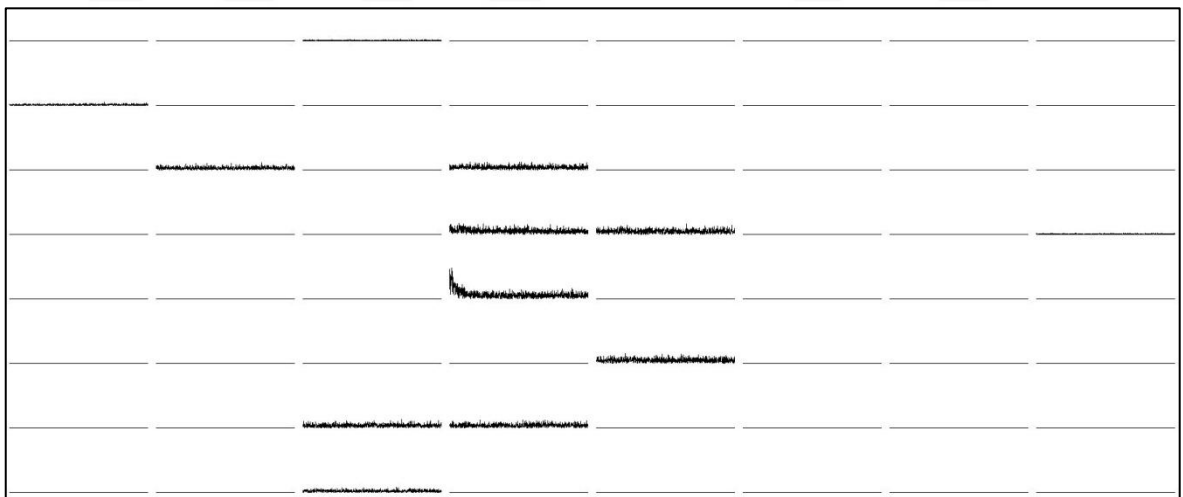
Figure 4.24 An 8x8 ^{31}P-MR spectroscopic free induction decay (FID) data of a volunteer which was acquired with compressed sensing.

^{31}P-MR spectroscopic dataset of a volunteer which was either fully acquired or accelerated using compressed sensing are shown in Figure 4.25. The result of accelerated ^{31}P-MR

spectroscopic dataset using compressed sensing was observed to be similar with original dataset, when the metabolite peak distributions were examined.
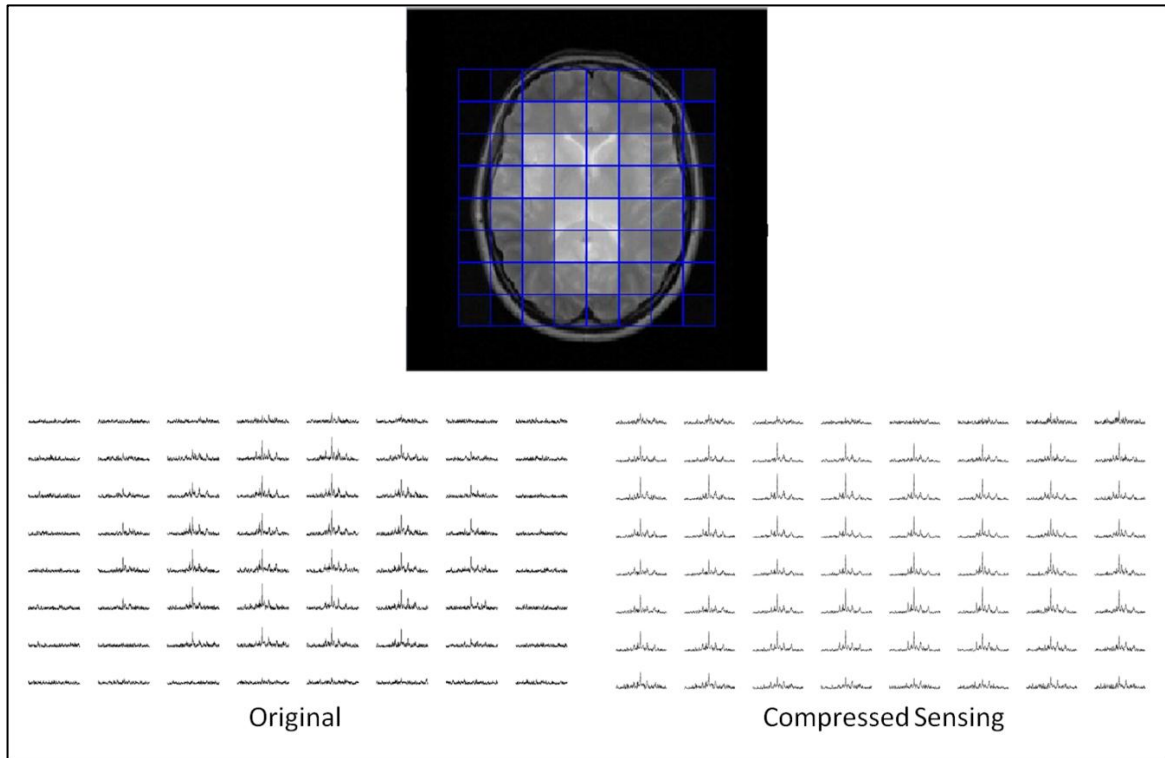
Figure 4.25 Fully acquired and the compressed sensing reconstructed ^{31}P-MR spectroscopic data of a volunteer.

Table 4.7 shows the Pi/PCr, PCr/PE and PCr/β-ATP ratios of original (O) and compressed sensing (CS) datasets of a volunteer. Pi/PCr and PCr/PE ratios of original and CS datasets were similar. Due to the lower β-ATP peak height, estimation of this peak is difficult, and therefore, PCr/β-ATP ratios of original and compressed sensing datasets have shown difference.

Table 4.7 Metabolite peak ratios of original (O) and compressed sensing (CS) datasets of a volunteer.

	Pi/PCr	PCr/PE	PCr/β-ATP
O	0.3±0.1	4.1±1.2	2.5±0.7
CS	0.2±0.03	3.6±0.6	3.6±1.7

Bland Altman test results of a volunteer are shown in Table 4.8. As a result of this analysis, Pi/PCr ratio of compressed sensing dataset of a volunteer was observed to have only one outlier with a small mean difference and standard deviation, while PCr/PE and PCr/β-ATP ratios have few outliers with large mean difference and standard deviation.

Table 4.8 Bland Altman test result for the similarity of the original and the compressed sensing datasets of a volunteer.

Bland Altman test result	Pi/PCr	PCr/PE	PCr/β-ATP
#outliers	1	1	2
mean (difference)	0.17	1.07	1.39
std (difference)	0.10	0.83	1.61

Figure 4.25 shows ^{31}P-MR spectroscopic dataset of a brain tumor patient which was fully acquired and accelerated using compressed sensing. The result of accelerated ^{31}P-MR spectroscopic dataset using compressed sensing was observed to be quite similar with original dataset. A few signal distortions were occurred in compressed sensing dataset, due to the high reduction factor.
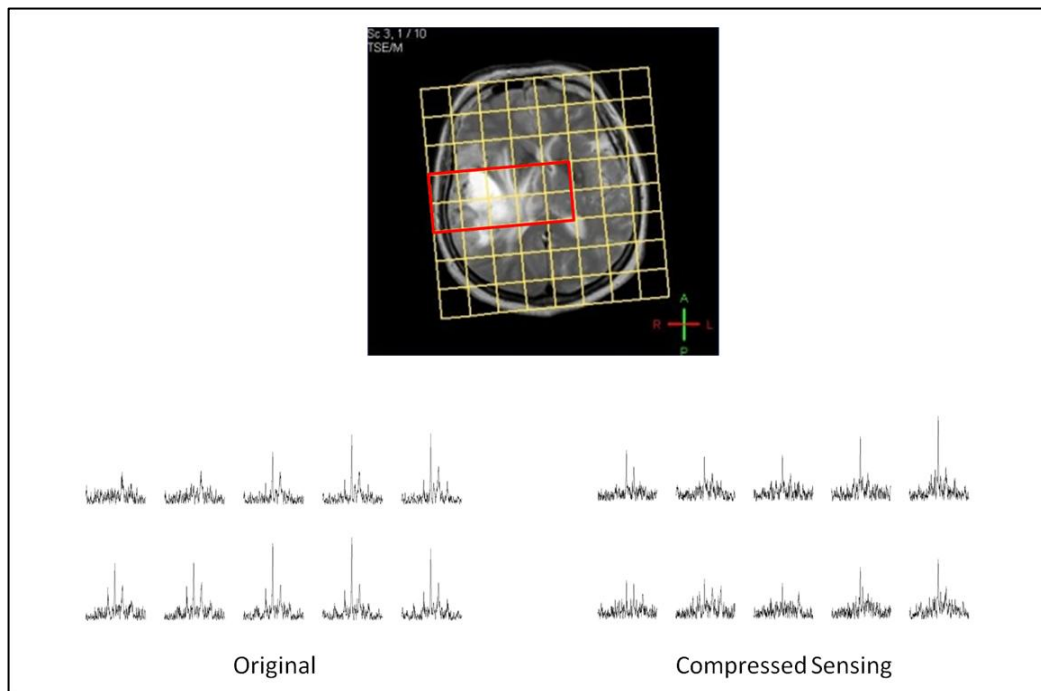
Figure 4.26 Fully acquired and compressed sensing reconstructed ^{31}P-MR spectroscopic data of a patient.

Tumor over healthy ratio of mean metabolite peak values for original and compressed sensing datasets can be seen in Table 4.9. Compressed sensing and original datasets had similar values in Pi and β-ATP peaks, while PCr peak difference between tumor and healthy was not similar with original dataset, due to the lower PCr peak in tumor region. Table 4.10 shows metabolite ratios of tumor and healthy for original and compressed sensing datasets of a patient. PCr/β-ATP ratios of tumor and healthy regions were similar in compressed sensing dataset. PCr peak height decreases in tumor region and as a result Pi/PCr ratio increases and PCr/PE ratio decreases in tumor. Both original and compressed sensing datasets showed the same trend.

Table 4.9 Tumor over healthy ratios of mean metabolite peaks of original and compressed sensing (CS) datasets of a patient.

Tumor/Healthy Ratio of Mean Metabolite Peak	PCr	Pi	β-ATP
Original	0.62	1.11	1.28
CS	1.01	1.20	0.96

Table 4.10 Metabolite ratios in tumor and healthy regions of the original and compressed sensing datasets of a patient.

	Tumor			Healthy		
	Pi/PCr	PCr/β-ATP	PCr/PE	Pi/PCr	PCr/β-ATP	PCr/PE
O (mean±std)	0.47±0.16	1.51±0.52	2.05±0.63	0.28±0.15	2.99±0.39	2.82±0.97
CS (mean±std)	0.23±0.07	2.87±1.04	1.99±0.53	0.19±0.05	2.67±0.53	2.57±0.37

SNR values of PCr, Pi and β-ATP peaks can be seen in Table 4.11. The denoising effect of compressed sensing inherently filters low magnitude peaks which include Pi and β-ATP peaks. This results in an unintentional loss of Pi and β-ATP peak heights, and therefore a lower SNR, contrary to what is expected. Table 4.12 shows the Bland Altman result of a patient. No outliers were observed in Pi/PCr ratios, and mean difference and standard deviation were small between original and CS datasets. PCr/β-ATP and PCr/PE ratios in tumor, and PCr/PE ratios in healthy regions were observed to have large mean differences and standard deviations.

Table 4.11 The SNR values of metabolite peaks in tumor and healthy regions of the original and compressed sensing datasets of a patient.

SNR (mean±std)	CS			O		
	PCr	Pi	β-ATP	PCr	Pi	β-ATP
Tumor	15.44±4.9	3.3±0.7	5.5±0.5	9.6±2	4.7±2.2	6.8±2.2
Healthy	15.4±3.7	2.8±0.7	5.7±0.7	14.4±2.7	3.9±1.7	5±1.2
Tumor/Healthy	1.0	1.17	0.95	0.66	1.21	1.39

Table 4.12 Bland Altman test results for the number of outliers, bias and std(bias) for the similarity of the peak ratios the original and compressed sensing datasets of a patient.

Bland Altman Test Result		Pi/PCr	PCr/β-ATP	PCr/PE
Tumor	# outliers	0	0	0
	mean(difference)	0.24	1.74	0.56
	std(difference)	0.15	0.66	0.75
Healthy	# outliers	0	0	1
	mean(difference)	0.13	0.59	0.74
	std(difference)	0.08	0.42	0.72

5. DISCUSSION

The aim of this study was to investigate the feasibility of compressed sensing reconstruction for accelerated ^{31}P-MR spectroscopic imaging of human brain tumors. SparseMRI software package was modified and improved for accelerating ^{31}P-MRSI using MATLAB. Some main and sub-functions of compressed sensing reconstruction algorithm were modified to work with 3 dimensions instead of 2 dimensions. With these modifications, even higher reduction factor resulted in closer results to the original ^{31}P-MRSI data. According to the results of Bland Altman and rank sum statistical tests, the optimal undersampling patterns were chosen for all sizes. Required changes were implemented into the Philips Paradise environment to be able to undersample the data. The appropriate undersampling patterns were used to acquire ^{31}P-MRSI data with pulse and acquire sequence in 3T Philips MR scanner. A volunteer and a patient with brain tumor were scanned to compare the fully acquired and compressed sensing accelerated ^{31}P-MRSI datasets.

In previous studies, compressed sensing technique was used to accelerate MR and MRS imaging for various purposes. Akcakaya et. al., Rapacchi et. al., and Makhijani et. al. studied on accelerated MR imaging [41-43]. Brain and prostate cancer were examined using accelerated ^{1}H-MRS imaging with compressed sensing [44-46]. The most detailed compressed sensing studies were implemented for ^{13}C-MRSI [8-10]. And finally, Parasoglou et. al. have studied on fast ^{31}P-MR spectroscopic imaging of human lower leg muscles [12]. However compressed sensing technique was mostly applied in k_z-k_t plane. Hu et. al. have performed compressed sensing technique in 3 dimensions [8].

Statistical test results of volunteer, and brain tumor patient datasets showed that compressed sensing reconstruction reduce the scan time while preserving the SNR due to its denoising effect. Compressed sensing reconstruction worked successfully in our study. However, some problems arose when tumor patient was scanned that resulted with signal loss in one side of the brain. Due to the high reduction factor, some artifacts and shift problems occurred. In future studies, optimization of compressed sensing undersampling patterns and reconstruction parameters will be done, and randomly generated

undersampling patterns will be performed. Additionally, compressed sensing technique will be implemented for other MR spectroscopic methods.

REFERENCES

1. Nelson, S.J., *Multivoxel magnetic resonance spectroscopy of brain tumors.* Mol Cancer Ther, 2003. 2(5): p. 497-507.

2. Hubesch, B., Sappey-Marinier, D., Roth, K., Meyerhoff, D.J., Matson, G.B., and Weiner, M.W., *P-31 MR spectroscopy of normal human brain and brain tumors.* Radiology, 1990. 174(2): p. 401-9.

3. Maintz, D., Heindel, W., Kugel, H., Jaeger, R., and Lackner, K.J., *Phosphorus-31 MR spectroscopy of normal adult human brain and brain tumours.* NMR Biomed, 2002. 15(1): p. 18-27.

4. Alger, J.R., Frank, J.A., Bizzi, A., Fulham, M.J., DeSouza, B.X., Duhaney, M.O., Inscoe, S.W., Black, J.L., van Zijl, P.C., Moonen, C.T., and et al., *Metabolism of human gliomas: assessment with H-1 MR spectroscopy and F-18 fluorodeoxyglucose PET.* Radiology, 1990. 177(3): p. 633-41.

5. Obruchkov, S., *Echo Planar Spectroscopic Imaging and 31P In Vivo Spectroscopy.* , in *Open Access Distertations and Theses. Paper 4121.,*2011, McMaster University.

6. Ulrich, M., Wokrina, T., Ende, G., Lang, M., and Bachert, P., *31P-{1H} echo-planar spectroscopic imaging of the human brain in vivo.* Magn Reson Med, 2007. 57(4): p. 784-90.

7. Srinivasa Raghavan, R.P., A.; Valette, J. ; James, J. R.; Heberlein, K.; Boettcher, U.; Henry P-G.; Bansal, N.; Dydak, U. *31P Spectroscopic Imaging with GRAPPA.* in *Conference Proceedings of 17th International Society of Magnetic Resonance in Medicine*. 2009. Hawaii, USA.

8. Hu, S., Lustig, M., Balakrishnan, A., Larson, P.E., Bok, R., Kurhanewicz, J., Nelson, S.J., Goga, A., Pauly, J.M., and Vigneron, D.B., *3D compressed sensing for highly accelerated hyperpolarized (13)C MRSI with in vivo applications to transgenic mouse models of cancer.* Magn Reson Med, 2010. 63(2): p. 312-21.

9. Hu, S., Lustig, M., Chen, A.P., Crane, J., Kerr, A., Kelley, D.A., Hurd, R., Kurhanewicz, J., Nelson, S.J., Pauly, J.M., and Vigneron, D.B., *Compressed sensing for resolution enhancement of hyperpolarized 13C flyback 3D-MRSI.* J Magn Reson, 2008. 192(2): p. 258-64.

10. Larson, P.E., Hu, S., Lustig, M., Kerr, A.B., Nelson, S.J., Kurhanewicz, J., Pauly, J.M., and Vigneron, D.B., *Fast dynamic 3D MR spectroscopic imaging with compressed sensing and multiband excitation pulses for hyperpolarized 13C studies.* Magn Reson Med, 2011. 65(3): p. 610-9.

11. Askin, N.C., Atis, B., and Ozturk-Isik, E., *Accelerated phosphorus magnetic resonance spectroscopic imaging using compressed sensing.* Conf Proc IEEE Eng Med Biol Soc, 2012. 2012: p. 1106-9.

12. Parasoglou, P., Feng, L., Xia, D., Otazo, R., and Regatte, R.R., *Rapid 3D-imaging of phosphocreatine recovery kinetics in the human lower leg muscles with compressed sensing.* Magn Reson Med, 2012. 68(6): p. 1738-46.

13. Webster, J.G., *Encyclopedia of Medical Devices and Instrumentation, 4 Volume Set.* 1988. 3022.

14. Bronzino, J.D., *The Biomedical Engineering Handbook.* 1999: CRC Press. 1656.

15. Coyne, K. *MRI: A Guided Tour.* [cited 2014 07 August]; Available from: http://www.magnet.fsu.edu/education/tutorials/magnetacademy/mri/fullarticle.html.

16. Enderle, J., Blanchard, S., and Bronzino, J., *Introduction to Biomedical Engineering.* 2005: Academic Press. 1144.

17. Brandao, L.A., *Neuroimaging Clinics of North America. MR spectroscopy of the brain. Preface.* Neuroimaging Clin N Am, 2013. 23(3): p. xiii-xiv.

18. Star-Lack, J., Nelson, S.J., Kurhanewicz, J., Huang, L.R., and Vigneron, D.B., *Improved water and lipid suppression for 3D PRESS CSI using RF band selective inversion with gradient dephasing (BASING).* Magn Reson Med, 1997. 38(2): p. 311-21.

19. Tran, T.K., Vigneron, D.B., Sailasuta, N., Tropp, J., Le Roux, P., Kurhanewicz, J., Nelson, S., and Hurd, R., *Very selective suppression pulses for clinical MRSI studies of brain and prostate cancer.* Magn Reson Med, 2000. 43(1): p. 23-33.

20. Ozturk-Isik, E., Crane, J.C., Cha, S., Chang, S.M., Berger, M.S., and Nelson, S.J., *Unaliasing lipid contamination for MR spectroscopic imaging of gliomas at 3T using sensitivity encoding (SENSE).* Magn Reson Med, 2006. 55(5): p. 1164-9.

21. Park, I., Larson, P.E., Zierhut, M.L., Hu, S., Bok, R., Ozawa, T., Kurhanewicz, J., Vigneron, D.B., Vandenberg, S.R., James, C.D., and Nelson, S.J., *Hyperpolarized 13C magnetic resonance metabolic imaging: application to brain tumors.* Neuro Oncol, 2010. 12(2): p. 133-44.

22. Larson, P.E., Bok, R., Kerr, A.B., Lustig, M., Hu, S., Chen, A.P., Nelson, S.J., Pauly, J.M., Kurhanewicz, J., and Vigneron, D.B., *Investigation of tumor hyperpolarized [1-13C]-pyruvate dynamics using time-resolved multiband RF excitation echo-planar MRSI.* Magn Reson Med, 2010. 63(3): p. 582-91.

23. Golman, K., Olsson, L.E., Axelsson, O., Mansson, S., Karlsson, M., and Petersson, J.S., *Molecular imaging using hyperpolarized 13C.* Br J Radiol, 2003. 76 Spec No 2: p. S118-27.

24. Kohler, S.J., Yen, Y., Wolber, J., Chen, A.P., Albers, M.J., Bok, R., Zhang, V., Tropp, J., Nelson, S., Vigneron, D.B., Kurhanewicz, J., and Hurd, R.E., *In vivo 13 carbon metabolic imaging at 3T with hyperpolarized 13C-1-pyruvate.* Magn Reson Med, 2007. 58(1): p. 65-9.

25. Star-Lack, J., Spielman, D., Adalsteinsson, E., Kurhanewicz, J., Terris, D.J., and Vigneron, D.B., *In vivo lactate editing with simultaneous detection of choline, creatine, NAA, and lipid singlets at 1.5 T using PRESS excitation with applications to the study of brain and head and neck tumors.* J Magn Reson, 1998. 133(2): p. 243-54.

26. Gupta, R.K., Cloughesy, T.F., Sinha, U., Garakian, J., Lazareff, J., Rubino, G., Rubino, L., Becker, D.P., Vinters, H.V., and Alger, J.R., *Relationships between*

choline magnetic resonance spectroscopy, apparent diffusion coefficient and quantitative histopathology in human glioma. J Neurooncol, 2000. 50(3): p. 215-26.

27. Robertson, N.J., Cox, I. J. , *Magnetic resonance spectroscopy of the neonatal brain.* [cited 2014 09 August]; Available from: http://www.mrineonatalbrain.com/ch04-16.php.

28. Ordidge, R., Connelly, A., and Lohman, J.A. , *Image-selected in vivo spectroscopy (ISIS): A new technique for spatially selective NMR spectroscopy.* J Magn Reson Imaging, 1986. 66: p. 283-294.

29. Salibi, N., Brown, M.A. , *Clinical MR Spectroscopy First Principles.* 1998: Wiley-Liss, Inc.

30. Candes, E.J., Romberg, J. , *Practical signal recovery from random projections.* in Proc. SPIE Computational Imaging, 2005.

31. Candes, E., Romberg, J., and Tao, T. , *Stable signal recovery from incomplete and inaccurate measurements.* Communications on Pure and Applied Mathematics, 2005. 59(8): p. 1207-1223.

32. Candes, E., Romberg, J., and Tao, T. , *Robust uncertainty principles: exact signal reconstruction from highly incomplete frequency information.* IEEE Transaction Information Theory, 2006. 52(2): p. 489-509.

33. Lustig, M., Donoho, D., and Pauly, J.M., *Sparse MRI: The application of compressed sensing for rapid MR imaging.* Magn Reson Med, 2007. 58(6): p. 1182-95.

34. Bertero, M., Boccacci, P. , *Introduction to Inverse Problems in Imaging. .* 1998, Bristol and Philadelphia: IOP Publishing Ltd.

35. Sarkar, T., Weiner, D., and Jain V. , *Some mathematical considerations in dealing with the inverse problem. .* IEEE Trans Antennas and Propogation, 1981. AP-29(2):373-379.

36. Hestenes, M., Stiefel, E. , *Methods of Conjugate Gradients for Linear Systems.* Journal of Research of the National Breau of Standards, 1952. 49(6):2379.

37. Shewchuk, J. , *An introduction to the conjugate gradient method without the agonizing pain.* 1994.

38. Vanhamme, L., Van Huffel, S., Van Hecke, P., and Van Ormondt, D. , *Time-domain quantification of series of biomedical magnetic resonance spectroscopy signals.* J Magn Reson, 1999. 140(1): p. 120-30.

39. Hatay, G.H., Gumus, C., Hakyemez, B., and Ozturk-Isik, E. , *Accelerated Phosphorus MR Spectroscopic Imaging of Human Brain Using Compressed Sensing.* in *International Society of Magnetic Resonance in Medicine.* 2013. Salt Lake City, UT: ISMRM.

40. Hatay, G.H., Okeer, E., Hakyemez, B., and Ozturk-Isik, E. , *Comparison of 2D Iterative Frame Based and 3D Direct Compressed Sensing Reconstruction for Accelerated Phosphorus MR Spectroscopic Imaging of Human Brain.* in *International Society of Magnetic Resonance in Medicine.* 2014. Milan, Italy.

41. Akcakaya, M., Rayatzadeh, H., Basha, T.A., Hong, S.N., Chan, R.H., Kissinger, K.V., Hauser, T.H., Josephson, M.E., Manning, W.J., and Nezafat, R., *Accelerated late gadolinium enhancement cardiac MR imaging with isotropic spatial resolution using compressed sensing: initial experience.* Radiology, 2012. 264(3): p. 691-9.

42. Makhijani, M.K., Balu, N., Yamada, K., Yuan, C., and Nayak, K.S., *Accelerated 3D MERGE carotid imaging using compressed sensing with a hidden Markov tree model.* J Magn Reson Imaging, 2012. 36(5): p. 1194-202.

43. Rapacchi, S., Han, F., Natsuaki, Y., Kroeker, R., Plotnik, A., Lehrman, E., Sayre, J., Laub, G., Finn, J.P., and Hu, P., *High spatial and temporal resolution dynamic contrast-enhanced magnetic resonance angiography using compressed sensing with magnitude image subtraction.* Magn Reson Med, 2014. 71(5): p. 1771-83.

44. Geethanath, S., Baek, H.M., Ganji, S.K., Ding, Y., Maher, E.A., Sims, R.D., Choi, C., Lewis, M.A., and Kodibagkar, V.D., *Compressive sensing could accelerate 1H MR metabolic imaging in the clinic.* Radiology, 2012. 262(3): p. 985-94.

45. Menzel, M.I., Tan, E.T., Khare, K., Sperl, J.I., King, K.F., Tao, X., Hardy, C.J., and Marinelli, L., *Accelerated diffusion spectrum imaging in the human brain using compressed sensing.* Magn Reson Med, 2011. 66(5): p. 1226-33.

46. Thomas, M.A., Nagarajan, R., Huda, A., Margolis, D., Sarma, M.K., Sheng, K., Reiter, R.E., and Raman, S.S., *Multidimensional MR spectroscopic imaging of prostate cancer in vivo.* NMR Biomed, 2014. 27(1): p. 53-66.

APPENDIX A

Algorithm A.1. MATLAB Simulated P31 MRSI Signal

```matlab
function data = create_simulated_signal(N)
tn=0.000333*[0:1023];
%Simulated 50 ms 500 ms 3200ms 4000 ms
% PCr gATP aATP bATP GPC GPE Pi PCh PE
%N=16;
fk=[0 -124 -387 -826 152 179 248 321 349];
dk=[30 30 30 30 30 30 30 30 30];
ak=[1.990 1.263 1.237 0.581 0.8609 1.166 0.6315 0.9384 0.6136];
ph=[0 0 0 0];
yn=0;

%Simulated 50 ms 500 ms 3200ms 4000 ms
fk_t=[0 -124 -387 -826 152 179 248 321 349];
dk_t=[30 30 30 30 30 30 30 30 30];
ak_t=[0.990 1.263 1.237 0.581 1.8609 2.166 0.9315 1.9384 1.6136];
ph_t=[0 0 0 0];
yn_t=0;

for n=1:size(ak,1)
    for m=1:size(ak,2)
        yn=yn+(ak(n,m)*exp(i*ph(n)*180/pi)*exp((-dk(n,m)+i*2*pi*fk(n,m))*tn));

    end
end
for n=1:size(ak_t,1)
    for m=1:size(ak_t,2)
        yn_t=yn_t+(ak_t(n,m)*exp(i*ph_t(n)*180/pi)*exp((-
dk_t(n,m)+i*2*pi*fk_t(n,m))*tn));
    end
end

yn_f=fftshift(fft(yn));
yn_tf=fftshift(fft(yn_t));

noise_1 = rand([1,1024])*max(abs(yn_f(:)))*0.3;
yn_f = yn_f+noise_1;
noise_2 = rand([1,1024])*max(abs(yn_tf(:)))*0.3;
yn_tf = yn_tf+noise_2;


data=zeros(N,N,1024);
for m=1:N
    for n=1:N
        if (m<=(N/2) & n<=(N/2))
            data(m,n,:)=yn_tf;
        elseif m>(N/2)
            data(m,n,:)=yn_f;
        elseif m<=(N/2) & n>(N/2)
            data(m,n,:)=yn_f;
        end
    end
end
end
```

Algorithm A.2. MATLAB P31 MRSI 3D Direct Compressed Sensing Reconstruction Simulation

```matlab
clear all;
close all;
addpath(strcat(pwd,'/utils'));
addpath(strcat(pwd,'/Wavelab850'));

WavePath;
size_xy=8;
p31= create_simulated_signal(size_xy);
p31_f = fftshift(fftn(p31));
figure; imshow(squeeze(abs(p31_f(:,:,513))), [0 max(abs(p31_f(:)))]);
figure; plot(squeeze(abs(p31_f(4,4,:))));
p31_rec= ifftn(ifftshift(p31_f));

%Select lines for zeros and create arrays with some random
%undersampling
p31_fu=p31_f;

load mask_2D_8_for2D_zero0.75_mid0.075_2.mat
%mask_2D=random_samp_2D(size_xy,size_xy,0.75);
R_factor = (size_xy*size_xy)/length(find(mask_2D>0));
for t=1:1024
    mask_all(:,:,t)=mask_2D;
end
figure; imagesc(mask_2D), axis image, colormap gray,
p31_fu=p31_f.*mask_all;

p31_fu_rec= ifftn(ifftshift(p31_fu));

im_z = p31_fu;
mask = mask_all;
data = im_z;
pdf = mask;
%%%%%%%%%%%%%%%%%%%%%%%%%%%%
% L1 Recon Parameters
%%%%%%%%%%%%%%%%%%%%%%%%%%%%

N = size(data);     % image Size
DN = size(data);    % data Size
TVWeight = 0.001;   % Weight for TV penalty
xfmWeight = 0.001;  % Weight for Transform L1 penalty
Itnlim = 15;        % Number of iterations

ham=hamming(6)*hamming(6)';

    for h=1:size(ham)
        ham1(:,:,h)=ham;
    end

    phmask = zpad3(ham1,N(1),N(2),N(3)); %mask to grab center frequency
    phmask = phmask/max(phmask(:));          %for low-order phase estimation and
correction
    ph = exp(i*angle((ifft3c(data.*phmask)))); % estimate phase for phase correction

%generate Fourier sampling operator
FT = p2DFT(mask, N, ph, 2);

% scale data
im_dc = FT'*(data);%.*mask);%./pdf);
data = data/max(abs(im_dc(:)));
im_dc = im_dc/max(abs(im_dc(:)));

%generate transform operator
XFM = Wavelet('Daubechies',4,4);   % Wavelet

% initialize Parameters for reconstruction

param = init;
param.FT = FT;
```

```matlab
param.XFM = XFM;
param.TV = TVOP;
param.data = data;
param.TVWeight =TVWeight;      % TV penalty
param.xfmWeight = xfmWeight;   % L1 Wavelet penalty
param.Itnlim = Itnlim;


res = XFM*im_dc;

% do iterations
tic
for n=1:5
    res = fnlCg(res,param);
    im_res = XFM'*res;

end
toc

p31_res=fftshift(im_res);


figure; imshow(squeeze(abs(p31_res(:,:,513))), [0 max(abs(p31_res(:)))]);
figure; plot(squeeze(real(p31_res(size_xy/4,size_xy/4,:))));

m=4;n=4;

figure; subplot(3,1,1);plot(squeeze(real(p31(m,n,:))))
hold on; subplot(3,1,2);plot(squeeze(real(p31_fu_rec(m,n,:))))
hold on; subplot(3,1,3);plot(squeeze(real(p31_res(m,n,:))))

figure, plot(squeeze(real(p31_res(4,4,:))),'k','LineWidth',2), axis([0 1024 0 1]);
box off
```